

1 **In-situ Observation of Riming in Mixed-Phase Clouds using the PHIPS**
2 **probe**

3 Fritz Waitz^a Martin Schnaiter^{a,b} Thomas Leisner^a Emma Järvinen^a

4 ^a *Institute of Meteorology and Climate Research, Karlsruhe Institute of Technology, Karlsruhe,*
5 *Germany* ^b *schnaiTEC GmbH, Bruchsal, Germany*

6 *Corresponding author:* Fritz Waitz, fritz.waitz@kit.edu

7 ABSTRACT: Mixed-phase clouds consist of both supercooled liquid water droplets and solid ice
8 crystals. Despite having a significant impact on Earth's climate, mixed-phase clouds are poorly
9 understood and not well represented in climate prediction models. One piece of the puzzle is
10 understanding and parameterizing riming of mixed-phase cloud ice crystals, which is one of the
11 main growth mechanisms of ice crystals via the accretion of small, supercooled droplets. Especially
12 the extent of riming on ice crystals smaller than $500\ \mu\text{m}$ is often overlooked in studies - mainly
13 because observations are scarce. Here, we investigated riming in mixed-phase clouds during three
14 airborne campaigns in the Arctic, the Southern Ocean and US east coast. Riming was observed
15 from stereo-microscopic cloud particle images recorded with the Particle Habit Imaging and Polar
16 Scattering (PHIPS) probe. We show that riming is most prevalent at temperatures around -7°C ,
17 where, on average, 43% of the investigated particles in a size range from $100 \leq D \leq 700\ \mu\text{m}$ showed
18 evidence of riming. We discuss the occurrence and properties of rimed ice particles and show
19 correlation of the occurrence and the amount of riming with ambient microphysical parameters.
20 We show that riming fraction increases with ice particle size ($<20\%$ for $D \leq 200\ \mu\text{m}$, $35\text{-}40\%$ for
21 $D \geq 400\ \mu\text{m}$) and liquid water content (25% for $\text{LWC} \leq 0.05\ \text{g m}^{-3}$, up to 60% for $\text{LWC} = 0.5\ \text{g m}^{-3}$).
22 We investigate the ageing of rimed particles and the difference between "normal" and "epitaxial"
23 riming based on a case study.

24 1. Introduction

25 Mixed-phase clouds (MPCs), consisting of both supercooled liquid droplets and ice particles,
26 play a major role in the ~~life cycle of clouds~~ atmospheric hydrological cycle and the radiative balance
27 of the Earth (e.g. Korolev et al. 2017). Despite their widespread occurrence, mixed-phase cloud
28 processes are still rather poorly understood and represent a great source of uncertainty for climate
29 predictions (e.g. McCoy et al. 2016).

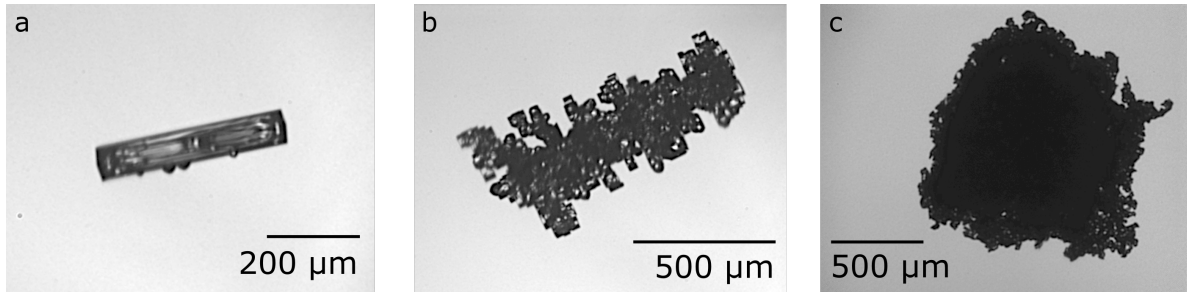
30 One important microphysical process in MPCs is *riming*, i.e. the accretion of small supercooled
31 liquid droplets on the surface of ice particles (see example in Fig. 1a). Besides vapor deposition
32 and aggregation, it is one of the three main ice growth modes.

33 Riming can be divided into two (not always easily distinguishable) sub-topics: riming of small ice
34 particles (diameter $D \simeq 100 - 1000 \mu\text{m}$) in clouds and riming of large ($1000 \lesssim D \lesssim 5000 \mu\text{m}$) pre-
35 cipitating ice, graupel ~~and snow particles~~, snow particles or frozen precipitation size droplets that
36 collect smaller cloud droplets or slower falling ice particles (e.g. "ice lollies" (Keppas et al. 2017)).
37 Whereas most recent publications focus on the latter aspect (riming of large precipitating particles),
38 in this study, we focus on riming of smaller ice particles in clouds.

39 The typical life-cycle of an exemplary rimed particle is usually as follows: The ice particle is
40 formed, ~~following~~ followed by growth via vapor deposition until the particle has reached a critical
41 minimum size for riming (depending on shape and habit, e.g. $D \geq 60 \mu\text{m}$ for columns, (e.g. Ono
42 1969; Ávila et al. 2009)). If liquid droplets are present in large enough numbers, the ice particle
43 starts collecting supercooled droplets (around $D = 10 - 40 \mu\text{m}$, e.g. Harimaya (1975)) that freeze
44 on the particle's surface ~~until~~. When the ice particles have acquired enough mass so gravitational
45 settling becomes efficient. ~~Whilst falling, the ice particle can~~, they precipitate and accrete even
46 more droplets whilst falling and grow further until it reaches the ground as graupel.

47 Ice particle growth, both in size and mass, can ultimately change cloud lifetime and radiative
48 properties. The scavenging of supercooled liquid water affects droplet size distribution and number
49 concentration and thus liquid water content as well as aerosol concentration (Baltensperger et al.
50 1998; Hegg et al. 2011). Also, splintering during the riming process can initiate secondary ice
51 formation, thus leading to the formation of new ice particles known as the *Hallett-Mossop-process*
52 (e.g. Hallett and Mossop 1974; Korolev et al. 2020; Field et al. 2017). Since rimed ice particles
53 are of higher mass and more compact compared to unrimed particles, their fall speed and terminal

54 velocity are increased (Locatelli and Hobbs 1974; Lin et al. 2011; Garrett and Yuter 2014).
 55 Furthermore, riming leads to increased surface roughness and complexity, and hence affects the
 56 ice particles' radiative properties, as shown in e.g. Schnaiter et al. (2016); Järvinen et al. (2018);
 57 Järvinen et al. (2021).



58 FIG. 1. Example of a (a) slight "normally" rimed , (b) heavily "~~epitactically~~epitaxially" rimed column and (c)
 59 a graupel particle captured by the PHIPS probe during the IMPACTS campaign.

60 In principle, riming can occur everywhere where ice particles and supercooled droplets coexist.
 61 ~~The riming efficiency of an ice particle is a function of (i) its collection efficiency and (ii) the~~
 62 ~~number of supercooled droplets, integrated over (iii) the time the ice particle spends in the cloud~~
 63 ~~and during precipitation. These three~~ Pflaum and Pruppacher (1979) have defined the collection
 64 kernel of a collector with radius R and a droplet with radius r that have a relative velocity Δv against
 65 each other as

$$66 \quad \underline{K = E_1 E_2 \pi (r + R)^2 \Delta v} \quad (1)$$

66 where E_1 is the collision efficiency of the two particles and E_2 the efficiency that the two particles
 67 remain attached to each other. Ice-ice collisions can lead to aggregation, droplet-droplet collisions
 68 to coalescence and ice-droplet collisions to riming. For riming, these quantities depend on nu-
 69 merous parameters including temperature (Kneifel and Moisseev 2020), ~~habit and size~~ humidity
 70 (Khain et al. 1999), habit, size and orientation of the ice particle (Ono 1969; Wang and Ji 2000;
 71 Ávila et al. 2009), ~~size~~ number and size distribution of the supercooled droplets (Saleeby and
 72 Cotton 2008) as well as turbulence and vertical velocity (Herzogh and Hobbs 1980; Garrett and
 73 Yuter 2014). The number of rime on an ice particle is hence dependent on all these quantities
 74 throughout particle's trajectory in the cloud and during precipitation.

75 In recent years, multiple studies have used radar measurements to retrieve information about
76 snow and riming density based on their vertical Doppler velocity (Mosimann et al. 1993; Leinonen
77 and Szyrmer 2015; Leinonen et al. 2018; Mason et al. 2018; Kneifel and Moisseev 2020). Those
78 methods proved to be fit to determine the riming state (i.e. whether a particle is rimed or unrimed)
79 of large, precipitating snow and graupel particles. However, they cannot resolve the fine structure
80 of small or freshly rimed ice particles inside clouds if the radar signal is dominated by large graupel
81 particles in the size range $D = 1 - 10$ mm. In-situ studies with high-resolution cloud imaging probes
82 investigating the properties of individual rimed particles sampled directly in the cloud, however, are
83 scarce. The difficulty is to resolve riming features and discriminate between rimed and non-rimmed
84 irregular particles. Furthermore, analysis of particle images is quite complex and hence automate
85 and manual assessment of particle properties is very laborious. Consequently, the riming of ice
86 particles is often times poorly or not at all represented in climate prediction models. So far, the
87 exact processes influencing the riming of could particles are not well understood. A deterministic
88 parameterization of when and where to expect how much riming does not exist. Most models
89 account for the riming degree (i.e. what fraction of a crystal's surface is covered by rime) only
90 in the sense of a *subtype* for hydrometeors (e.g. *cloud ice*, *graupel*, *snow*, COSMO, Blahak and
91 Seifert (2015), <http://www.cosmo-model.org/>). Furthermore, riming is neglected completely in
92 most Arctic model studies (e.g. Fan et al. 2011; Ovchinnikov et al. 2014; Stevens et al. 2018).

93 In this work, we investigate riming of ice particles using the Particle Habit Imaging and Polar
94 Scattering (PHIPS) probe. PHIPS is an aircraft-mounted cloud probe acquiring stereo-microscopic
95 images and corresponding angular scattering functions of single cloud particles in the size range
96 $D = 20 - 700 \mu\text{m}$ and $D = 50 - 700 \mu\text{m}$ for ice and droplets, respectively. With its high optical
97 resolution and single particle measurements, PHIPS is well suited to investigate detailed features
98 like riming of individual ice particles. We present microphysical observations of ice particles
99 from three field campaigns investigating high latitude MPC. In section 2, we give an overview of
100 the three field campaigns as well as a brief introduction of the PHIPS probe and its data analysis
101 methods. Combining the data from these three field campaigns, an extensive data-set observing
102 ice particles of various size, habit and riming state has been acquired. In section 3, we present
103 a statistical analysis of the correlation with ambient conditions of rimed particles for different
104 scales-degrees of riming. We estimate the minimum size of rimed particles as well as droplets,

105 confirming the results of previous laboratory studies. Further, we highlight various riming features
106 such as one-sided rimed plates or "ice lollies" (Keppas et al. 2017). One particularly interesting
107 observation is ice particles carrying small, faceted rime oriented to the crystalline axis of the host
108 particle. Such particles have been observed before (Korolev et al. 2020) but their occurrence and
109 properties have not been studied comprehensively. This type of riming, which we call *Epitaxial*
110 *Riming* and which is e.g. shown in Fig. 1b, will be analyzed in detail in section 4 including a case
111 study showing the typical step-by-step evolution of ~~epitactically~~ epitaxially rimed particles.

112 2. Methods and Experimental Data Set

113 a. Campaigns

114 In this work, we use experimental in-situ data gathered during three airborne field campaigns:

- 115 1. ACLOUD - Arctic CLOUD Observations Using airborne measurements during polar Day,
116 May/June 2017 based in Svalbard (Spitsbergen, Norway) with the AWI Polar6 aircraft
117 (165 flight hours),
- 118 2. SOCRATES - Southern Ocean Clouds, Radiation, Aerosol Transport Experimental Study,
119 Jan/Feb 2018 based in Hobart (Tasmania, Australia) with the NCAR Gulfstream-V aircraft
120 (105 flight hours) and
- 121 3. IMPACTS - Investigation of Microphysics and Precipitation for Atlantic Coast-Threatening
122 Snowstorms, Jan/Feb 2020 based in Wallops (VA, USA) with the NASA P3 aircraft (53 flight
123 hours).

124 An overview of the ~~meteorological and~~ microphysical conditions as well as the instrumentation
125 during those campaigns can be found in Knudsen et al. (2018) and Wendisch et al. (2019) for
126 ACLOUD, McFarquhar et al. (2019) for SOCRATES and McMurdie et al. (2019) for IMPACTS.
127 The sampling during those three campaigns includes a wide variety of different cloud conditions:
128 warm clouds, supercooled liquid clouds, ice clouds and mixed-phase clouds. Clouds sampled
129 ranged in altitude from boundary layer clouds below 200 m to mid-level clouds between 4000 m
130 and 6000 m asl. Temperatures ranged from -20 to +5°C during ACLOUD, -35 to +5°C during
131 SOCRATES and -32 to +9°C during IMPACTS. The sampled ice particles covered a wide range
132 of different particle shapes and habits (columns, plates, needles, bullet rosettes, dendrites and

133 irregulars, including rough, rimed and pristine particles) as well as sizes from $D = 20 - 700 \mu\text{m}$.
134 The instrumentation on the three aircraft included cloud particles probes such as the SID-3 (*Small*
135 *Ice Detector Mk. 3*), CDP (*Cloud Droplet Probe*, DMT, Longmont, USA), CIP (*Cloud Imaging*
136 *Probe*, DMT, Longmont, USA) and PIP (*Precipitation Imaging Probe*, DMT, Longmont, USA)
137 during ACLOUD, 2D-C, 2D-S (*Two-dimensional Stereo Probe*, *Two-dimensional Cloud Probe*,
138 SPEC Inc., Boulder, USA) and CDP during SOCRATES and 2D-S, CDP and CPI (*Cloud Particle*
139 *Imager*, SPECinc, Boulder, CO, USA) during IMPACTS.

140 For SOCRATES, vertical Doppler velocity was measured by the HCR (HIAPER cloud Radar,
141 UCAR/NCAR-EOL (2022)) which has a transmit frequency 94.40 GHz (W-band), temporal
142 resolution 10 Hz, vertical range resolution of 20 to 180 m and a typical radial velocity uncertainty
143 of 0.2 m s^{-1} at a vertical velocity of $w = 2 \text{ m s}^{-1}$). The velocity data is corrected for aircraft motion
144 and aliasing-bias. The ambient temperature was measured with a heated temperature sensor (Harco
145 149 Model 100009-1 Deiced TAT) that has a general accuracy of 0.3°C . The vertical velocity was
146 measured using a Radome air-motion system (UCAR/NCAR-Earth Observing Laboratory 2019)

147 . Relative humidity was measured by the VCSEL (Vertical-Cavity Surface-Emitting Laser
148 hygrometer) with an uncertainty ranging from 6% to 10% (Diao 2021). During ACLOUD, the
149 temperature was measured using an open-wire Pt100 in an unheated Rosemount housing at the
150 tip of the noseboom with a frequency of 100 Hz and an estimated accuracy of $\pm 0.1^\circ\text{C}$. The
151 vertical wind was measured using a Rosemount 858 five-hole probe with a relative accuracy of
152 the vertical wind speed of $\pm 0.05 \text{ m/s}$ for straight and level flight sections. During IMPACTS,
153 atmospheric state measurements were performed using the Rosemount Total Air Temperature
154 (TAT) probe and the Edgetech three-stage chilled mirror hygrometer with 1 Hz temporal resolution
155 (Martin and Bennett 2020). For each PHIPS particle, the corresponding temperature, humidity
156 and velocity data as well as LWC were determined as the average over $t = t_s \pm 0.5 \text{ s}$ around the time
157 of acquisition t_s where each PHIPS particle was sampled.

158 Due to the variability of the ~~meteorological~~ microphysical conditions and sampled particles,
159 the data gathered during these three campaigns provide a suitable and representative data set for
160 a comprehensive characterization of riming in mixed-phase clouds. All data cited in this work
161 can be found in the corresponding data bases for the three campaigns: Ehrlich et al. (2019) for
162 ACLOUD, EOL (2018) for SOCRATES, McMurdie et al. (2019) for IMPACTS.

163 *b. The PHIPS Probe*

164 PHIPS is designed to investigate the microphysical and light scattering properties of cloud par-
165 ticles. It produces microscopic stereo-images whilst simultaneously measuring the corresponding
166 angular scattering function for the angular range from 18° to 170° for single cloud particles. More
167 information and a detailed characterization of the PHIPS setup and instrument properties can be
168 found in depth in Abdelmonem et al. (2016) and Schnaiter et al. (2018). From the stereo images,
169 single-particle microphysical features such as e.g. area equivalent diameter or aspect ratio, can
170 be obtained. The image analysis algorithm is explained in depth in Schön et al. (2011). Based
171 on the single-particle's angular scattering function, the thermodynamic phase and the scattering
172 equivalent diameter can be derived as explained in Waitz et al. (2021).

173 For ACLOUD and SOCRATES, the instrument settings were set to measure single cloud particles
174 in a size range from $50 \mu\text{m} \leq D \leq 700 \mu\text{m}$ and $20 \mu\text{m} \leq D \leq 700 \mu\text{m}$ for droplets and ice particles,
175 respectively. The image acquisition rate of the microscopic system was limited to 3 Hz in these
176 campaigns, while single-particle scattering data could be acquired up to a maximum rate of 3.5 kHz.
177 The magnification settings of the cameras corresponded to an optical resolution of approximately
178 $3.3 \mu\text{m}$. Since PHIPS characterizes individual particles, it has a narrow sensitive area (A_{sens}). As
179 discussed in Waitz et al. (2021), A_{sens} is size dependent (e.g. $A_{\text{sens}} = 0.5 \text{ mm}^2$ for ice particles with
180 $D = 200 \mu\text{m}$). Assuming a relative flight speed of $v_s = 150 \text{ m s}^{-1}$, this corresponds to a sampling
181 volume of $V_{\text{sens}} = A_{\text{sens}} \cdot v_s = 0.08 \text{ L s}^{-1}$. During IMPACTS, the scientific focus was on larger ice
182 crystals so the trigger threshold as well as the magnification were increased to trigger only particles
183 larger than $D \geq 100 \mu\text{m}$ for droplets and $D \geq 40 \mu\text{m}$ for ice. The magnification settings of the
184 cameras corresponded to an optical resolution of approximately $4 \mu\text{m}$ and the maximum camera
185 acquisition rate was varied between 3 to 10 Hz, which corresponds to a maximum spatial resolution
186 of roughly one stereo-image per 15 m.

187 *c. Manual Image Classification*

188 All PHIPS stereo-images from the ACLOUD and SOCRATES data-set were visually classified
189 into seven habit classes: (i) plate-like particles (single plates, sectorized plates, skeleton plates and
190 side planes), (ii) columnar particles (solid columns, hollow columns and sheaths), (iii) needles,
191 (iv) frozen droplets, (v) bullet rosettes, (vi) graupel, and (vii) irregular particles. In addition to

192 the habits, the particles were assigned the attributes ~~(i) aggregate, (ii) rimed or (iii) pristine.~~ The
193 rimed or unrimed. The temperature dependent frequency of occurrence distribution of the different
194 particle habits are shown in the SI (~~FigsFig. S1 and S2~~)for the two campaigns). An overview of the
195 riming fraction and riming type (normal, epitaxial, see Sec. 4) per habit is shown in Fig. ~~S3~~S2.

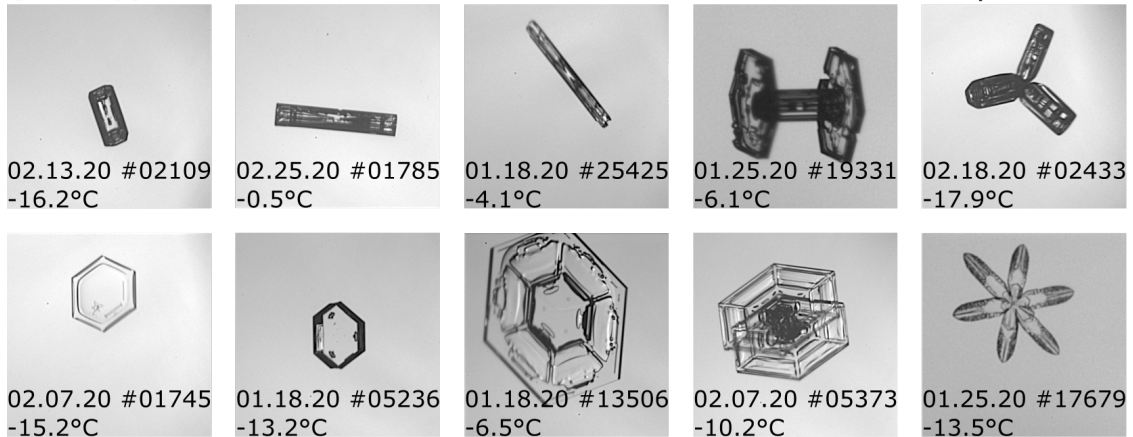
196 In a next classification step, a subset of the well classified particles was again visually classified
197 further regarding their riming features. The second classification step was performed only for
198 particles larger than 100 μm sampled at a temperature $> -17^\circ\text{T} \geq -17^\circ\text{C}$. Smaller particles were
199 almost exclusively small irregulars whose riming state could not be classified with certainty due
200 to the limited optical resolution and almost no riming was observed at lower temperatures, see
201 Fig.4a. CDP LWC ranged from 0 g/m³ to 0.5 g/m³ and vertical HCR Doppler velocity from -4 m/s
202 to +2 m/s.

203 Particles were classified regarding their surface riming degree (SRD) as (i) unrimed (SRD = 0%,
204 no visible riming on any of the two stereo-micrographs), (ii) slightly rimed (SRD < 25%, a few
205 scattered ~~droplets on the particle~~rime particles on the crystal's surface), (iii) moderately rimed
206 (25% \leq SRD \leq 50%, up to half of the particle's surface is covered by ~~droplets~~rime), (iv) heavily
207 rimed (50% < SRD \leq 100%, most ~~or all~~ of the particle's surface is covered by rime) as well as (v)
208 graupel (SRD \gg 100%, the whole particle surface is covered by multiple layers of rime, so that
209 the structure of the underlying particle is no longer recognizable). Exemplary PHIPS particles from
210 these classes are shown in Figs. 2 and 3. This classification approach is similar to the definition
211 of riming degree used in previous studies such as Magono and Lee (e.g. 1966); Brintjes et al.
212 (e.g. 1987); Mosimann et al. (e.g. 1993, 1994); Mosimann (e.g. 1995). Also, the attributes (i)
213 ~~sublimated, (ii) one-sided~~one-sided riming and ~~(iii)~~iii epitaxial riming (which will be explained in
214 detail in section 4) were assigned. As each particle is imaged from two different viewing angles
215 (120° apart), whether or not a particle has rime only on one side can also be assessed for opaque
216 particles (see examples in Fig. 6).

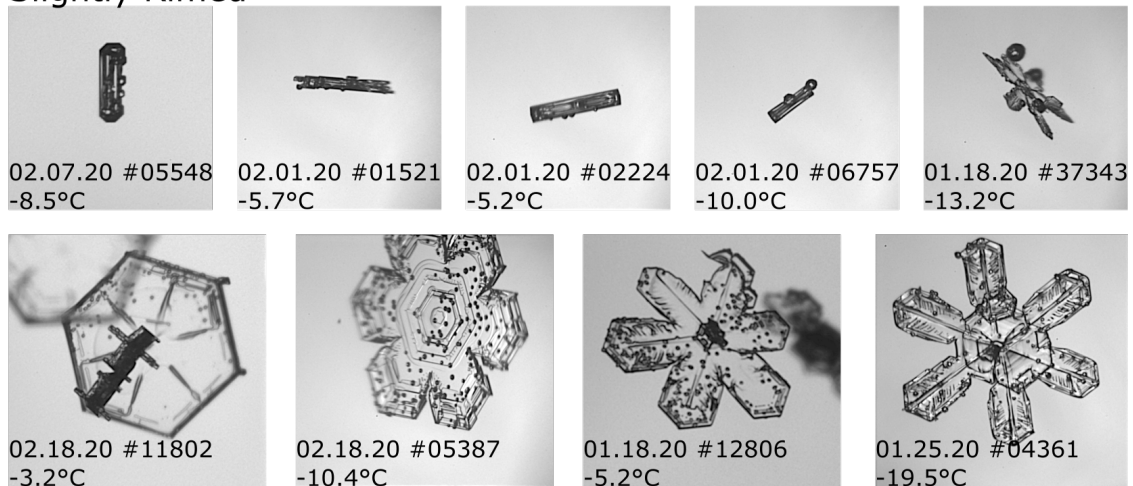
217 The remaining data-set includes 3,957 particles from ACLOUD and 1,413 from SOCRATES.
218 Examples of particles classified in the different categories are shown in the following section.
219 Manual classification was not applied for the complete IMPACTS data set due to large number of
220 ice particle images (over 250,000 images were acquired). Therefore, only the set of images used
221 for the case study presented in section b was manually inspected.

Unrimed

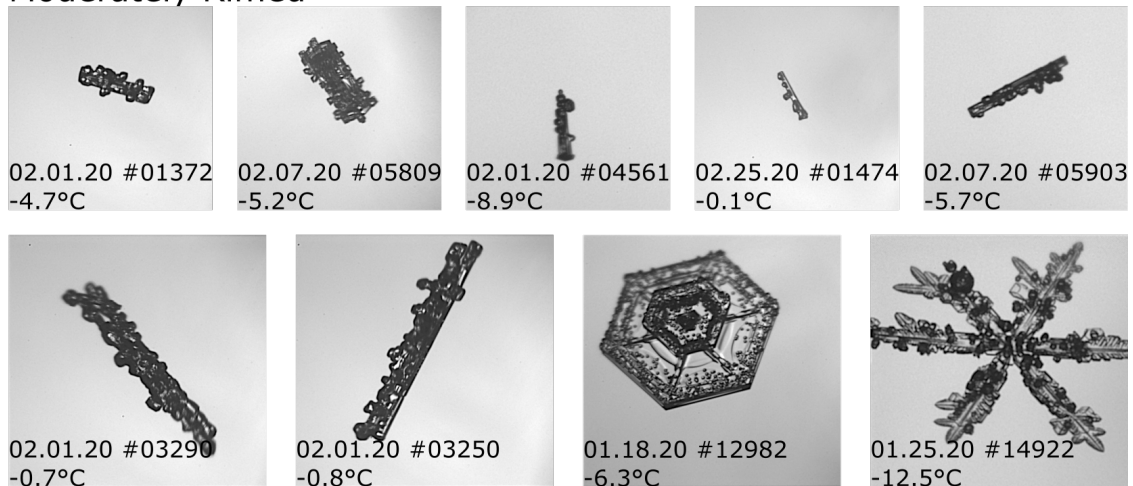
500 μm 



Slightly Rimed

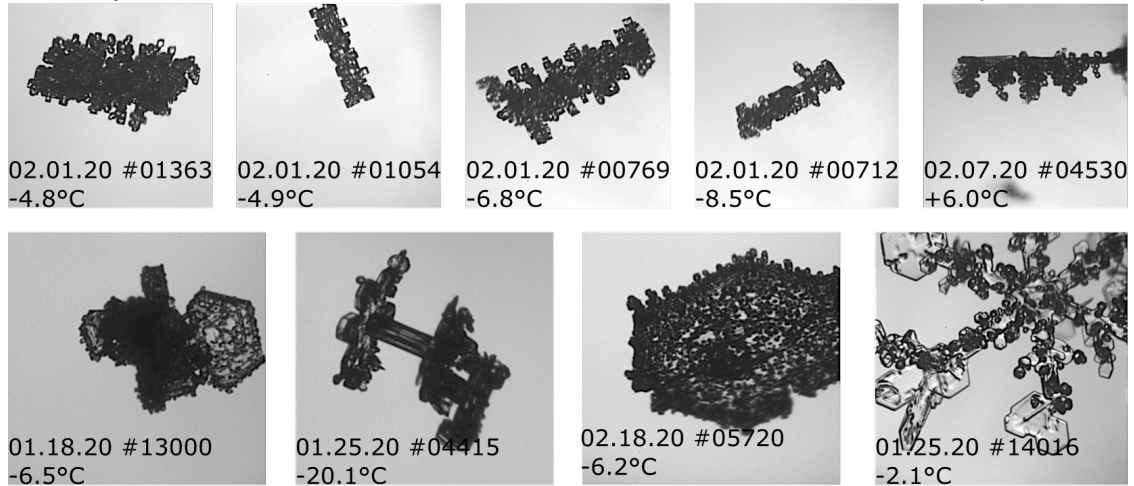


Moderately Rimed

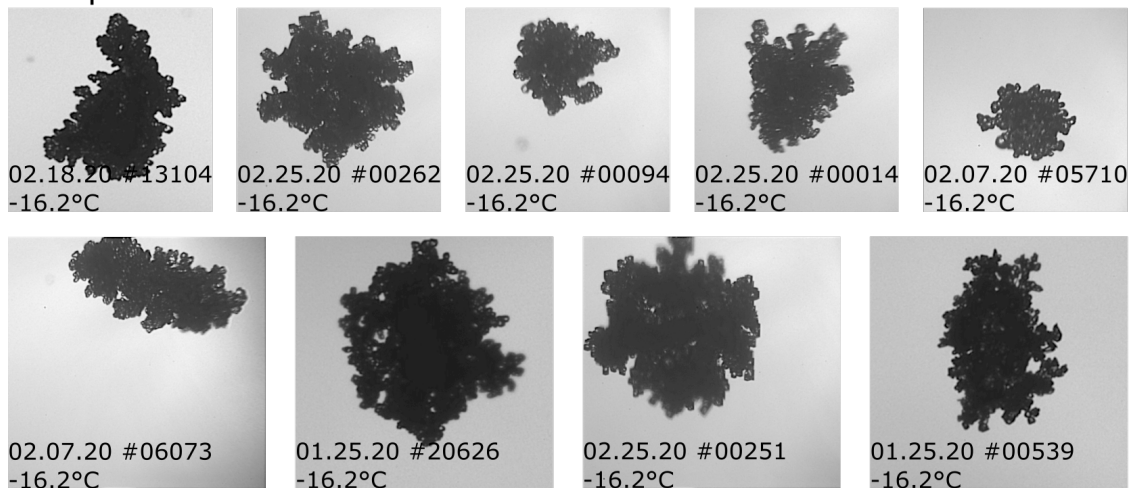


222 FIG. 2. Examples of representative PHIPS particles with different degrees of riming categorized by the
 223 surface riming degree (SRD): unrimed (SRD=0%), slightly rimed (0% < SRD < 25%) and moderately rimed
 224 (25 ≤ SRD ≤ 50%) particles. Heavily rimed (50% < SRD < 100%) and graupel particles (SRD = 100%) are
 225 shown in Fig. 3.

Heavily Rimed



Graupel



226 FIG. 3. Examples of representative PHIPS particles with different degrees of riming depending on the surface
227 riming degree (SRD): heavily rimed ($50\% < \text{SRD} < 100\%$) and graupel particles ($\text{SRD} = 100\%$). Unrimed
228 ($\text{SRD} = 0\%$), slightly rimed ($0\% < \text{SRD} < 25\%$) and moderately rimed particles ($25 \leq \text{SRD} \leq 50\%$) are shown
229 in Fig. 2.

230 3. Statistical Analysis and Correlation with Ambient Conditions

231 In general, the average number of rime found on an ice particle is calculated as the integrated
232 riming rate over the particle trajectory. The riming rate is a function of the relative flux of
233 available droplets and hence droplet number concentration and relative velocity with respect to the
234 ice particle. Further, it is dependent on the collision probability (and hence the cross sections As
235 discussed in the introduction, riming is dependent on a variety of atmospheric quantities including

236 temperature, humidity and vertical wind velocity as well as trajectory and microphysical properties
237 such as number concentration, size distribution, habit and orientation of ice particles and droplets)
238 ~~as well as on the collection efficiency, i. e. the probability that a colliding droplet sticks as rime.~~
239 ~~The trajectory of the ice particle and thus the time it spends in the cloud is dependent on its mass~~
240 ~~and the vertical (updraft) velocity.~~

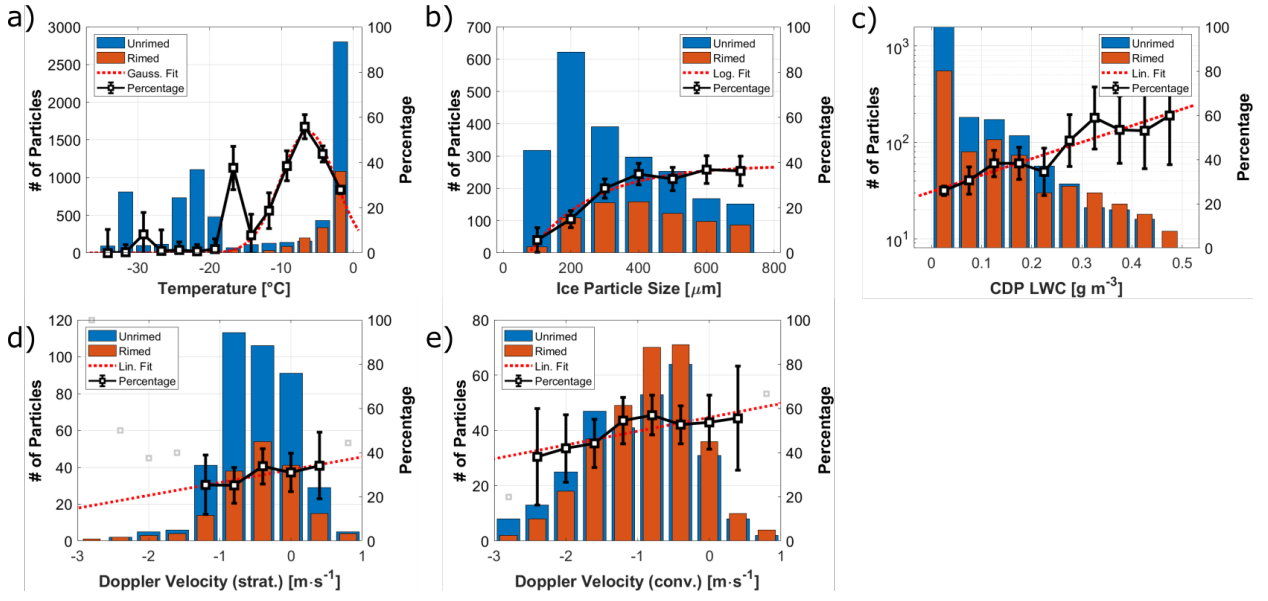
241 supercooled droplets. It is not possible to know each of those parameters for each particle at
242 every given moment. Hence, as already mentioned above, such detailed description of riming
243 on a particle-by-particle basis is not present in current climate prediction models and riming
244 is only accounted for in terms of graupel and snow and rarely for smaller, less densely rimed
245 particles. Here, we investigate riming of sub-millimeter ice particles based on ~~experimental in~~
246 situ aircraft data and correlate the relative occurrence of rimed and unrimed ice particles with
247 ~~ambient meteorological other~~ microphysical parameters. Note that the measured conditions do
248 not necessarily represent the environment where the particles ~~were rimed~~ experienced riming but
249 rather where they were sampled.

250 This statistic is based on 5,370 manually classified images from the ALOUD and SOCRATES
251 campaign. ~~Fig. 4a shows the correlation of riming fraction and ambient temperature. Here~~

252 a. Riming Fraction

253 In the following, "riming fraction" refers to the relative amount of rimed particles compared
254 to total amount of classified ice particles (rimed + unrimed). Fig. 4a shows the correlation of
255 riming fraction and ambient temperature. The corresponding fit parameters for all histograms are
256 shown in Table 1. Most riming was observed in a temperature range between $-10^{\circ}\text{C} \leq T \leq 0^{\circ}\text{C}$
257 with the maximum around $T \approx -7^{\circ}\text{C}$ where up to almost 5055% of all ice particles were rimed.
258 The high riming fraction around -17°C is due to a very high rimed fraction in this temperature
259 bin during a single cloud segment of RF09 of SOCRATES. It is based on a low number of total
260 particles ($n = 213$) and is therefore not assumed to be a generalizable feature. ~~The corresponding~~
261 ~~fit parameters for all histograms are shown in Table 1.~~

272 For the following analysis, apart from Fig. 4a, only particles sampled at $T \geq -17^{\circ}\text{C}$ are considered.
273 Fig. 4b shows riming statistics as a function of ice particle's area equivalent diameter retrieved from
274 the stereo-microscopic images. It can be seen that the percentage of rimed particles increases with



262 FIG. 4. Histograms showing the absolute number of classified unrimed (blue) and rimed (red) particles during
 263 ACLOUD and SOCRATES as well as the riming fraction (relative percentage $n_{\text{rimed}}/n_{\text{all}}$, black, right axis) in
 264 correlation with different ambient parameters: Temperature (a), area-eq. diameter of the underlying ice particle
 265 measured by PHIPS (b), CDP liquid water content (c) and vertical HCR Doppler velocity in stratiform (d) and
 266 convective clouds (e). HCR data is only available for SOCRATES. The red dotted line shows a fit to the riming
 267 fraction (see text right y-axis). The corresponding fit parameters for all histograms are shown in Tab. 1. The
 268 statistical uncertainty bars correspond to the number of particles per bin ($n^{-1/2}$). Only bins with $n \geq 20$
 269 are considered for the fit, others are shown in grey. Correlation plots with further parameters (CDP mean droplet
 270 diameter, ambient vertical velocity, relative cloud height, supersaturation with respect to ice relative humidity),
 271 which show only a weak dependency, are shown in Fig. S4-S3 in the SI.

275 particle size. The riming fraction increases from below 5% for particles smaller than $D_{\text{im,A}} \leq$
 276 $150 \mu\text{m}$ to over 35% for particles larger than $D_{\text{im,A}} \geq 400 \mu\text{m}$. Above that, the riming fraction
 277 is only weakly dependent on particle size. The smallest ice particle where riming was observed
 278 was a column with an area equivalent diameter of $D_{\text{im,A}} = 116.1 \mu\text{m}$ and maximum dimension
 279 $D_{\text{im,max}} = 193.7 \mu\text{m}$ (shown in Fig. S8-S7 in the SI). This is a larger riming onset size compared to
 280 e.g. Ono (1969); Ávila et al. (2009)) who reported a critical minimum diameter of $D \geq 60 \mu\text{m}$ for
 281 riming on columns collected via glass slides and analyzed by optical microscopy.

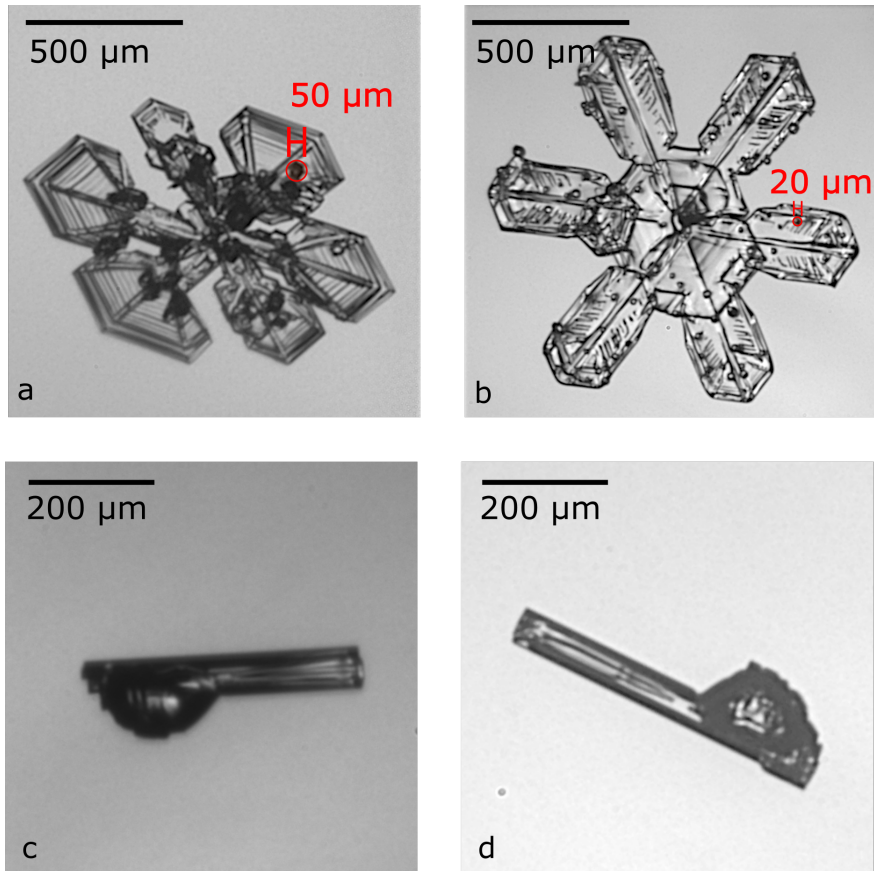
282 The correlation of riming fraction and cloud liquid water content (LWC) measured by the CDP
 283 is shown in Fig. 4c. The riming fraction increases from 25% in cloud segments with low LWC

TABLE 1. Fit parameters to the riming percentage histograms shown in Fig. 4.

		Fit function	R ²
Temperature		$y = -0.952 x^2 - 12.2 x + 11.9$	0.940
Ice particle diameter	(PHIPS)	$y = 38.7 - \exp[-52.8 (x-769)]$	0.964
Liquid water content	(CDP)	$y = 74.7 x + 25.5$	0.863
Vertical Doppler velocity	(HCR, strat.)	$y = 29.3 - 5.79 x + 32.7 - 32.2$	0.790 0.707
<u>Vertical Doppler velocity</u>	<u>(HCR, conv.)</u>	<u>$y = 6.24 x + 55.9$</u>	<u>0.724</u>

284 below 0.05 g m^{-3} to 60% for $\text{LWC} \geq 0.5 \text{ g m}^{-3}$. ~~Rimed droplets~~ Rime particles had a size around
 285 roughly $D_{\text{max}} \simeq 20$ and $50 \mu\text{m}$ as shown in Figs. 5a,b for two exemplary ~~particles~~ ice crystals that
 286 were amongst the crystals with the smallest and largest rime particles based on visual inspection.
 287 This is in agreement with results presented by e.g. Kikuchi and Uyeda (1979); Harimaya (1975),
 288 who reported sizes of ~~rimed droplets~~ rime particles between 10 and $60 \mu\text{m}$. As there exists no
 289 automated method to determine the size of the rime particles based on the PHIPS images, the size
 290 of rime particles is not further investigated in this work. Comparison with CDP mean droplet
 291 diameter showed a slight correlation with a maximum riming fraction at $D_{\text{drop, mean}} = 20 \mu\text{m}$ (see
 292 Fig. ~~S4f~~ S3f in the SI). Figs. 5c,d show drizzle-rimed ice (*ice lollies*). Such contact freezing of
 293 relatively large droplets compared to the size of ice particle was reported by (Uyeda and Kikuchi
 294 1978; Keppas et al. 2017). We also see this in our data set, but there are only very few cases. Due
 295 to the low number, no correlation with sampled PHIPS drizzle droplet concentration was found
 296 and no detailed statistical analysis was conducted.

299 Fig. 4d ~~shows and e show~~ the correlation with the Doppler radial velocity measured by the
 300 ~~HIAPER cloud Radar (HCR, UCAR/NCAR-EOL (2022)), HCR~~, which is the sum of vertical wind
 301 air velocity and particle fall speed, corrected by the vertical motion of the aircraft. ~~Negative~~
 302 ~~velocity corresponds to downward direction, positive to updrafts~~ HCR data are only available for
 303 the SOCRATES campaign. Since the HCR has a dead zone of 145 m around the aircraft in which
 304 data are not usable, there is no data available at the location of the aircraft. ~~One~~ Hence, each data
 305 point corresponds to the ~~average over the whole vertical column. HCR data are only available for~~
 306 ~~the SOCRATES campaign. measured HCR Doppler velocity of the first valid gate closest to the~~
 307 aircraft. The HCR was typically rotated to point in zenith direction when flying beneath clouds or
 308 ascending through boundary layer clouds and nadir at other times. The sign was adjusted based on
 309 HCR orientation so that negative velocity always corresponds to downward direction, positive to



297 FIG. 5. Exemplary slightly rimed particles showing the size of rimed droplets rime particles on the surface (a,
 298 b) and drizzle rimed ice (ice lollies, c,d).

310 upward direction. The analysis was divided into stratiform and convective cloud segments based
 311 on the flag given in UCAR/NCAR-EOL (2022). For stratiform cases, events for which the melting
 312 layer was close to the position of the aircraft were omitted, since events where in-situ probes and the
 313 first gate were not "on the same side" of the melting layer would lead to potentially biased velocities
 314 due to the discontinuity at the melting layer (Romatschke 2021; Romatschke and Dixon 2022). It
 315 can be seen, that there is a clear trend of increasing riming fraction towards more positive (up-
 316 ward) Doppler velocity with riming fraction. Due to the updraft, the ice velocities. Further,
 317 on average, the riming fraction is much higher in convective (52%) compared to stratiform
 318 clouds (34%). This can be explained by updrafts and in-cloud turbulence which increases
 319 the time and trajectory that the particles remain in the cloud longer and hence as well as the
 320 relative velocity of ice particles against droplets and thus increases the probability that they

321 collide ~~with droplets increases.~~ Previous studies have reported increased fall speeds for rimed
322 particles (Locatelli and Hobbs 1974; Lin et al. 2011; Garrett and Yuter 2014) which indicates that
323 ~~the particles are still in the cloud and not yet precipitating.~~ to form riming.

324 The measurement of ambient vertical velocity around the aircraft shows a slight correlation
325 towards both higher positive and negative values (see Fig. ~~S4h~~S3h in the SI). This could indicate
326 a correlation with turbulent air motion, as riming is expected to be more likely if particles remain
327 longer in the cloud, having a longer total travel path and hence a higher chance of collecting droplets.
328 However, at the same time, a lot of ~~one-sided~~one-sided rimed plates were observed during the
329 campaigns (see Fig. 6), which would be unlikely if all riming would necessarily be correlated with
330 turbulent air motion. This confirms observations of fallen snow by Ono (1969); Rango et al. (2003).
331 Note that the ambient vertical velocity measured at the aircraft is the combination of small-scale
332 turbulence and large-scale vertical motion which cannot be easily disentangled. Roughly 15% of
333 all plates at warm-high temperatures $T > -10^{\circ}\text{C}$ are ~~one-sided~~rimed on one side (see Fig. ~~S7a~~S6a
334 and the corresponding discussion in the SI) and almost none at ~~colder temperatures.~~

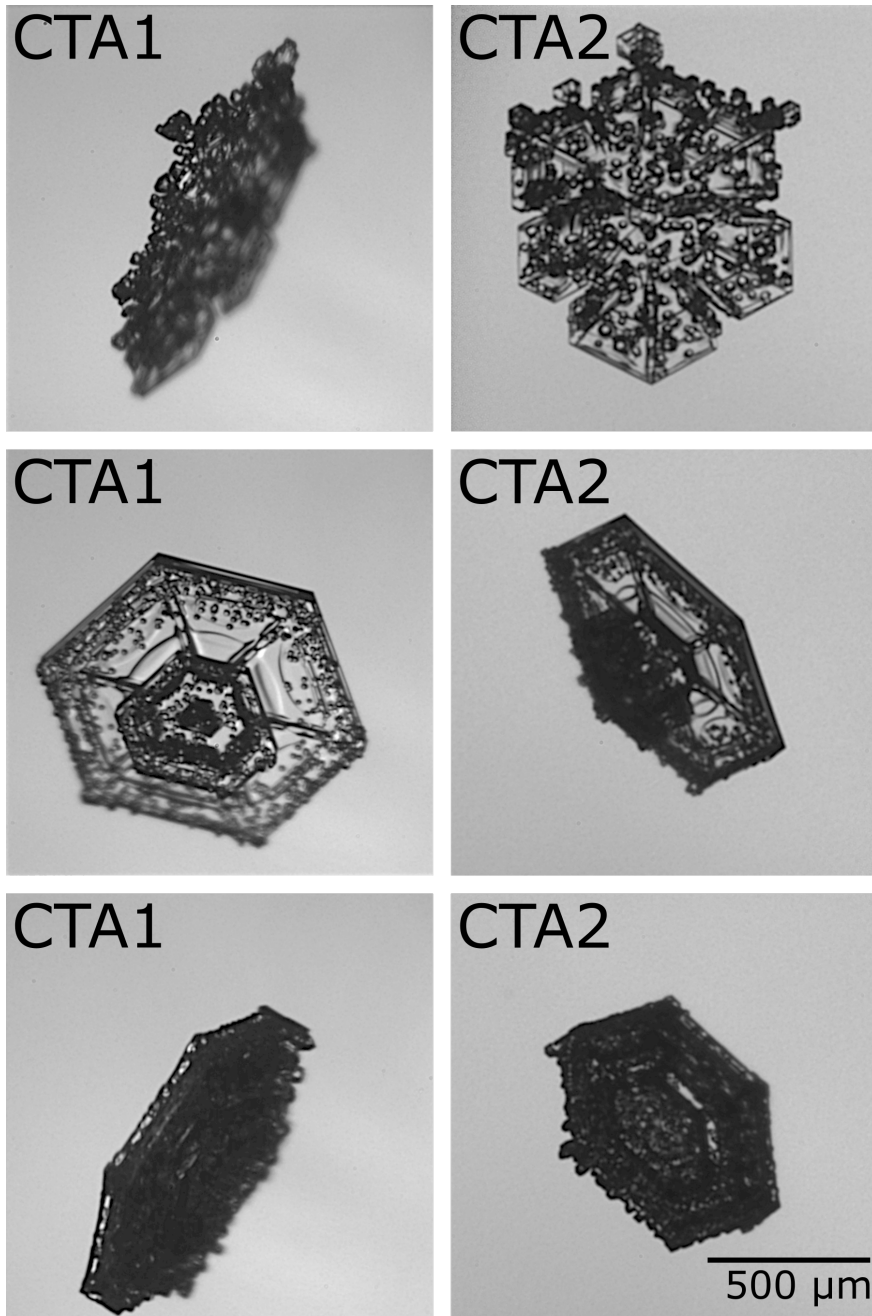
335 ~~Three exemplary one-sided rimed particles shown from different perspectives by the two camera~~
336 ~~telescope assemblies (CTA1 and CTA2). Note that the particle orientation in the stereo image does~~
337 ~~not reflect the orientation within the cloud.~~

338 lower temperatures. No significant correlation (R^2 below 0.5) or only very minor dependency
339 of riming fraction and CDP droplet number concentration, CDP mean droplet diameter, ambient
340 vertical velocity, relative cloud height and ~~supersaturation with respect to ice~~relative humidity
341 were found. The corresponding plots are shown in Fig. ~~S4~~S3 in the SI.

345 *b. Riming Degree*

346 All rimed ice particles were manually classified concerning their *riming degree*, i.e. their
347 estimated surface riming degree (~~SRD~~) ~~(see Sec. e).~~ This classification was done manually based
348 on visual inspection of the particle's individual stereo-images. Exemplary particles are shown in
349 Fig. 2.

350 ~~Examples of (1) columnar particles and (2) plates with different degrees of riming depending on~~
351 ~~the surface riming degree (SRD): unrimed (a, $\text{SRD} = 0\%$), slightly rimed (b, $0\% < \text{SRD} < 25\%$),~~



342 FIG. 6. Three exemplary one-sided, moderately rimed particles shown from different perspectives by the two
 343 camera telescope assemblies (CTA1 and CTA2). Note that the particle orientation in the stereo image does not
 344 reflect the actual orientation with respect to horizon.

352 moderately rimed (c, $25 \leq \text{SRD} \leq 50\%$), heavily rimed (d, $50\% < \text{SRD} \leq 100\%$) and graupel
 353 particle (e, $\text{SRD} \gg 100\%$).

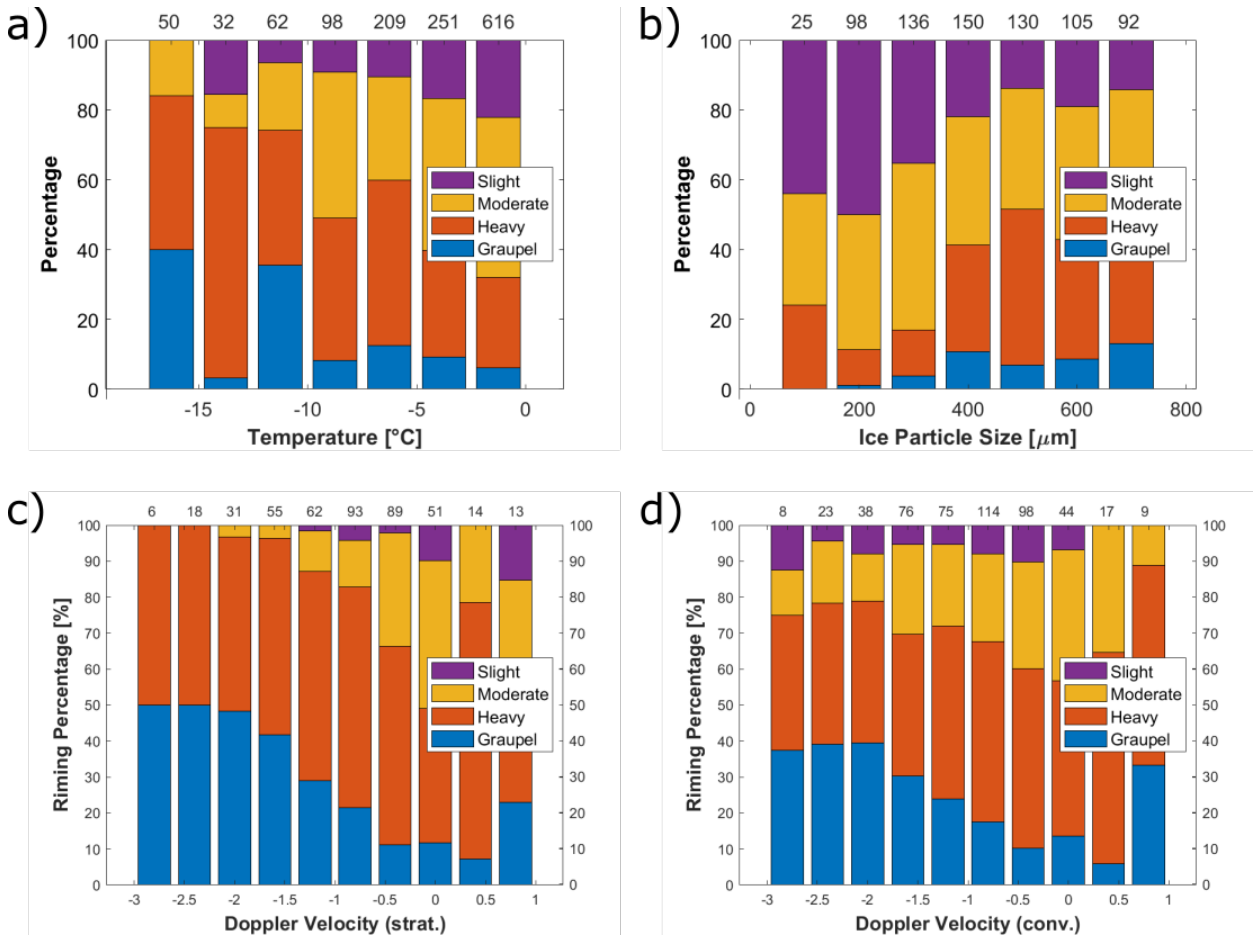
354 Fig. 7 shows the relative distribution of SRD with three ambient and microphysical parameters:
355 temperature (Fig. 7a), ice particle area equivalent diameter (Fig. 7b) and vertical Doppler velocity
356 (Fig. 7c). A correlation is seen between temperature and SRD. At ~~colder~~ lower temperatures
357 ice particles are more heavily rimed. At temperatures $T \leq -15^{\circ}\text{C}$, more than 80% of all rimed
358 particles are heavily rimed or graupel, whereas most slightly rimed particles are found at ~~warm~~
359 high temperatures between -5 and 0°C . ~~The relative fraction of heavily rimed particles is only~~
360 ~~moderately temperature dependent.~~

361 A positive correlation is also visible between SRD and ice particle size: Most small particles
362 around $D_{\text{im,A}} \leq 250 \mu\text{m}$ show only slight riming whereas heavy riming is mostly found on larger
363 particles. These typically large heavily rimed and graupel particles correlate with an increased
364 negative (downwards) Doppler velocity (Fig. 7c,d) as they are almost spherical and hence more
365 densely packed compared to aspherical ice particles. This is in agreement with Doppler radar
366 studies presented by Mosimann (1995). ~~However, apart from that, no correlation of SRD with~~
367 ~~vertical Doppler velocity is visible. The weak but positive trend of SRD and downward Doppler~~
368 ~~velocity presented by Mosimann (1995) is not seen here. This effect is weaker for convective clouds~~
369 (Fig. 7d) compared to stratiform clouds (Fig. 7c). A possible explanation is that the increased fall
370 speed due to the increase SRD cancels out with updrafts of the air parcels that cause the increased
371 SRD in the first place.

372 Comparisons with LWC and the other previously discussed parameters (plots shown in the SI)
373 show no apparent correlation. Since the classification of SRD is only based on visual inspection,
374 no further numerical analysis was conducted and no fit parameters are presented.

379 4. Epitaxial Riming

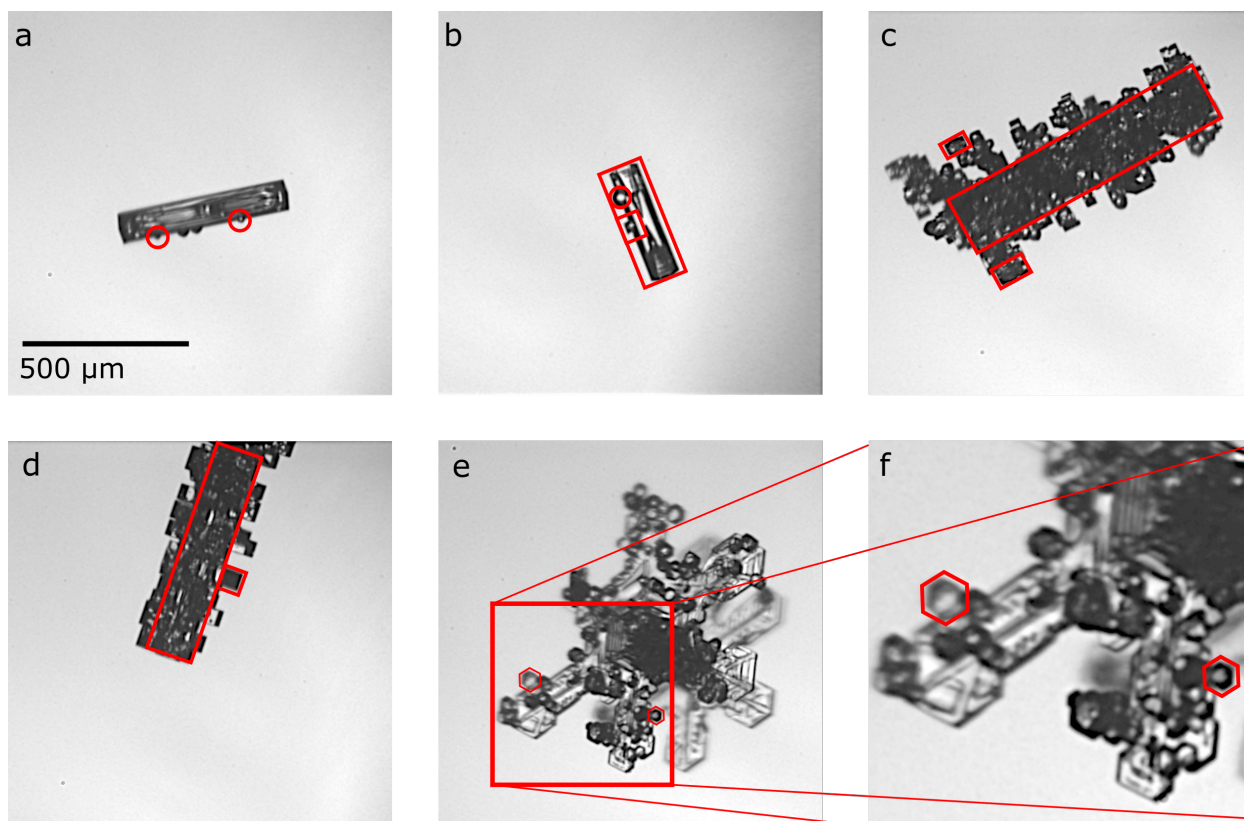
380 Rimed ice particles are usually understood as ice particles which have round accretion (rime).
381 However, during their ageing process, the form of accretion can change significantly. Fig. 8 shows
382 exemplary rimed ice particles with differently structured rime: round rime (Fig. 8a) and crystalline,
383 faceted rime (Fig. 8b-e). The latter can be explained by ageing (vapor deposition growth) of rimed
384 particles. In the following, round rime ~~on ice particles~~ particles on ice crystal surfaces will be
385 referred to as "*normal riming*".



375 FIG. 7. The relative occurrence of particles of different riming degree as defined in Fig. 2: slight (purple),
 376 moderate (yellow) and heavy riming (red) as well as graupel (blue) in correlation with ambient temperature
 377 (a), ice particle size (b), and HCR Doppler velocity (c,d) similar to Fig. 4a-e. The values on the upper x-axis
 378 correspond to the total number of particles per bin.

386 Particles with faceted rime have been reported in the past. Korolev et al. (2020) have reported
 387 a case study with "a few ice particles with small faceted particles stuck to their surfaces" which
 388 they refer to as "aged rimed ice particles" that had possibly originated from "vapor deposition
 389 regrowth of rime into faceted particles". Libbrecht (2016) has reported "oriented freezing" of
 390 ~~rimed droplets~~ rime particles that "freeze with their molecular lattices matching the pre-existing
 391 lattice underneath" which results in "faceted rime particles". Since not all aged rimed particles
 392 show small faceted particles on the surface and the attribute "faceted" is often used in other context
 393 for ice particles (pristine plates, e.g. Libbrecht et al. (2015); Korolev et al. (2020)), we propose the

394 term "*epitaxial riming*" to avoid any confusion. In general, epitaxy refers to crystalline growth of
395 a material on the surface of another particle along the lattice structure of the underlying particle
396 (Pashley 1956). The epitaxial growth of ice on the surface of crystalline substrates, such as e.g.
397 feldspar, has been the topic of many previous works (e.g. Bryant et al. 1960; Kiselev et al. 2016).
398 Here, we describe the growth of small ice particles on the surface of larger ice particles along the
399 same crystal axis. Thus, the term "*epitaxial riming*" refers to faceted, rimed particles, underlining
400 the important property that the small "rimed" particles on the surface inherit the same lattice
401 structure as the underlying host particle and share the same c-axis as shown in Fig. 8.



402 FIG. 8. Exemplary rimed ice particles sampled during the IMPACTS campaign: slightly, "normally rimed"
403 column (a), slightly rimed column with both normal and epitaxial riming (b), heavily epitaxially rimed columns
404 (c,d) and a moderately, epitaxially rimed plate (e).

405 Multiple studies exist investigating the orientation of crystallographic axes of the freezing of
406 rimed droplets rime particles, both in-vitro (Magono and Aburakawa 1969; Takahashi 1979; Mizuno
407 1984; Mizuno and Wakahama 1983) and in-situ (Uyeda and Kikuchi 1980). It has been shown

408 that the crystal structure of rimed (still round) droplets matches the underlying lattice structure. At
409 ~~warm-high~~ temperatures $-10 \leq T \leq 0^\circ\text{C}$, most small droplets ($D \lesssim 40 \mu\text{m}$) freeze as single crystals
410 whereas at ~~colder-lower~~ temperatures ($T \leq -15^\circ\text{C}$), ~~rimed droplets-rime particles~~ tend to freeze
411 as polycrystals. However, to our knowledge, so far no studies exist that analyze the properties
412 and formation conditions of the aforementioned epitaxially rimed particles. In the following, we
413 present detailed observations of such ice particles and propose that they are the result of vapor
414 deposition on rimed particles.

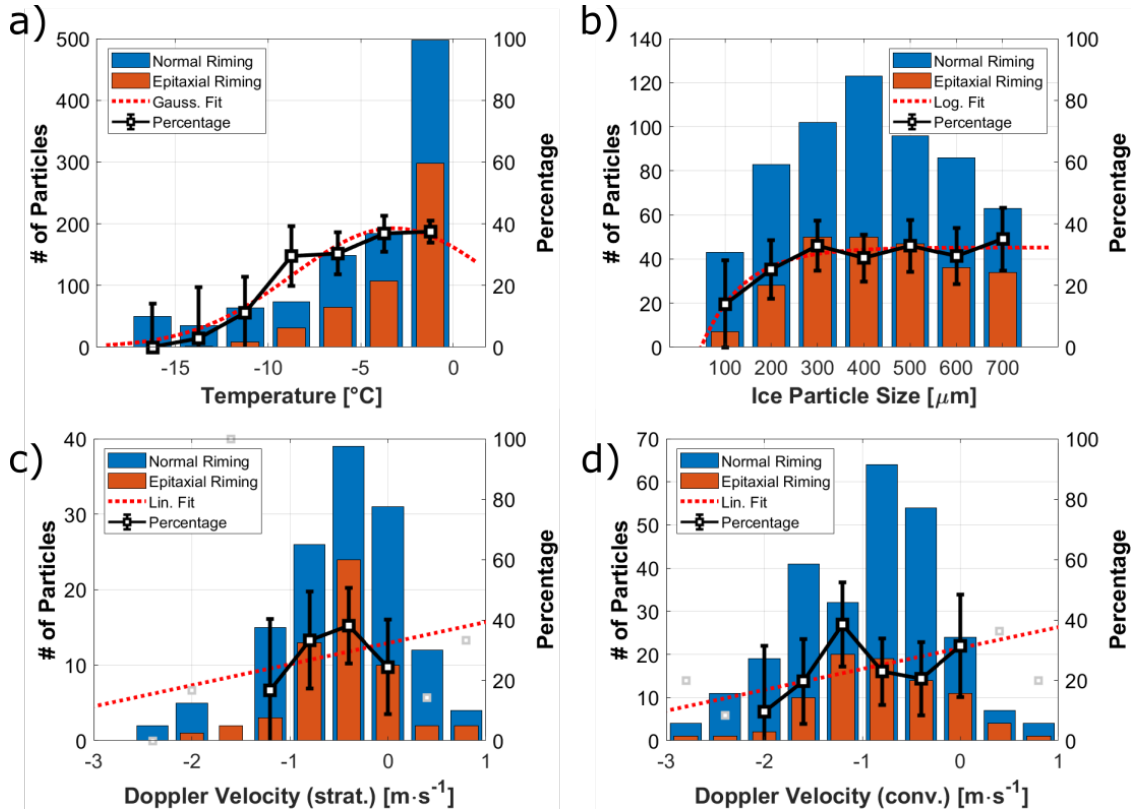
415 a. Correlation of Epitaxial Riming with Ambient Conditions

416 In Fig. 9, we show the relative occurrence of normally and epitaxially rimed particles during the
417 ACLOUD and SOCRATES campaign in correlation with ambient ~~meteorological-microphysical~~
418 parameters. The corresponding fit parameters for all histograms are shown in Tab. 2. Again, only
419 particles sampled at a temperature $T \geq -17^\circ\text{C}$ with diameter $D \geq 100 \mu\text{m}$ that were distinctively
420 classified according to the aforementioned manual classification are included.

425 Fig. 9a shows that there is a tendency to find more epitaxial riming at ~~warmer-higher~~ temperatures
426 near $T = 0^\circ\text{C}$, where up to almost 40% of all rimed particles show epitaxial riming. Between -5
427 and -10°C , the fraction of epitaxial riming slightly decreases from 40% to 30%. Below $T < -10^\circ\text{C}$,
428 the percentage of epitaxial riming decreases below 20%, although it should be noted that the
429 statistics for this temperature region are weak. This temperature dependency is in accordance with
430 the aforementioned studies showing that the ~~rimed droplets-rime particles~~ tend to freeze as single
431 crystals along the c-axis of the underlying particle.

432 Fig. 9b shows a slight correlation of the occurrence of epitaxial particles with the size of the
433 underlying particle. For small particles below $D \leq 150 \mu\text{m}$, the fraction of epitaxially rimed
434 particles is 20%. This increases to up to 40% for ice particles larger than $D \geq 300 \mu\text{m}$. ~~Above~~
435 ~~that~~For larger particles, the fraction of epitaxially rimed crystals is only weakly dependent of
436 particle size. The correlation of particle size with the presence of epitaxial riming can be explained
437 by the fact that epitaxial riming is caused by vapor deposition during the ageing process of rimed
438 particles which naturally also causes the particle to grow on their main surfaces.

439 ~~FigFigs. 9c shows a trend towards higher upwardvertical velocity and d show a trend of increasing~~
440 positive (upward) Doppler velocity with fraction of epitaxially rimed particles, indicating a corre-



421 FIG. 9. Absolute number of analyzed particles for normal (blue) and epitaxial (red) riming and fraction of
 422 epitaxially rimed particles as a function of ambient temperature (a), ice particle size (b) and HCR Doppler
 423 velocity for stratiform (c) and convective cloud segments (d). Only bins with more than $n \geq 20$ data points were
 424 taken into account ($n < 20$ are shown in grey).

441 lation with updrafts. We see no substantial difference between the stratiform and convective cases.
 442 Again, comparisons with LWC and the other previously discussed parameters show no significant
 443 correlation (plots shown in the SI).

444 Next, we will present a case study of a MPC sampled during the IMPACTS campaign. We
 445 investigate the assumption that the ice particles with epitaxial riming are the result of ageing of
 446 rimed particles and discuss its formation process.

TABLE 2. Fit parameters to the riming percentage histograms shown in Fig. 9.

		Fit function	R ²
Temperature		$y = -0.312 x^2 + -1.37 x + 36.6$	<u>0.93</u> <u>0.930</u>
Ice particle diameter	(PHIPS)	$y = 32.3 - \exp[-109 (x-367)]$	0.898
Vertical Doppler velocity	(HCR, strat.)	$y = 15.5 6.98 x + 18 32.3$	<u>0.856</u> <u>0.144</u>
<u>Vertical Doppler velocity</u>	<u>(HCR, conv.)</u>	<u>$y = 6.92 x + 30.7$</u>	<u>0.265</u>

447 *Case Study Feb01st – Epitaxial Riming on Columns*

448 *b. Case Study Feb01st - Epitaxial Riming on Columns*

449 Fig. ~~10a shows meteorological and~~ 10 shows microphysical data collected on February 1st during
 450 the 2020 IMPACTS campaign. The MPC segment discussed in this case study was probed from
 451 12:42:30 - 12:49:00 UTC ($\Delta t = 06:30$ min, which corresponds to $\Delta s = 58.5$ km) in an altitude of
 452 approximately 4,300 m at a temperature of about -12°C around $36^\circ\text{N}/73^\circ\text{W}$, roughly 300 km near
 453 the US east coast. The vertical wind velocity was at a constant value around $\pm 0 \text{ m s}^{-1}$. The
 454 relative humidity with respect to ~~ice averaged about 100~~ water averaged about 93%. The liquid
 455 water content (LWC) measured with the CDP averaged around 0.1 g m^{-3} and the total water
 456 content (TWC) measured with the 2DS was around 0.5 g m^{-3} . The number-weighted mean particle
 457 diameter was around $20 \mu\text{m}$ for droplets and between 200 to $800 \mu\text{m}$ for ice particles based on the
 458 measurements of CDP and 2D-S, respectively.

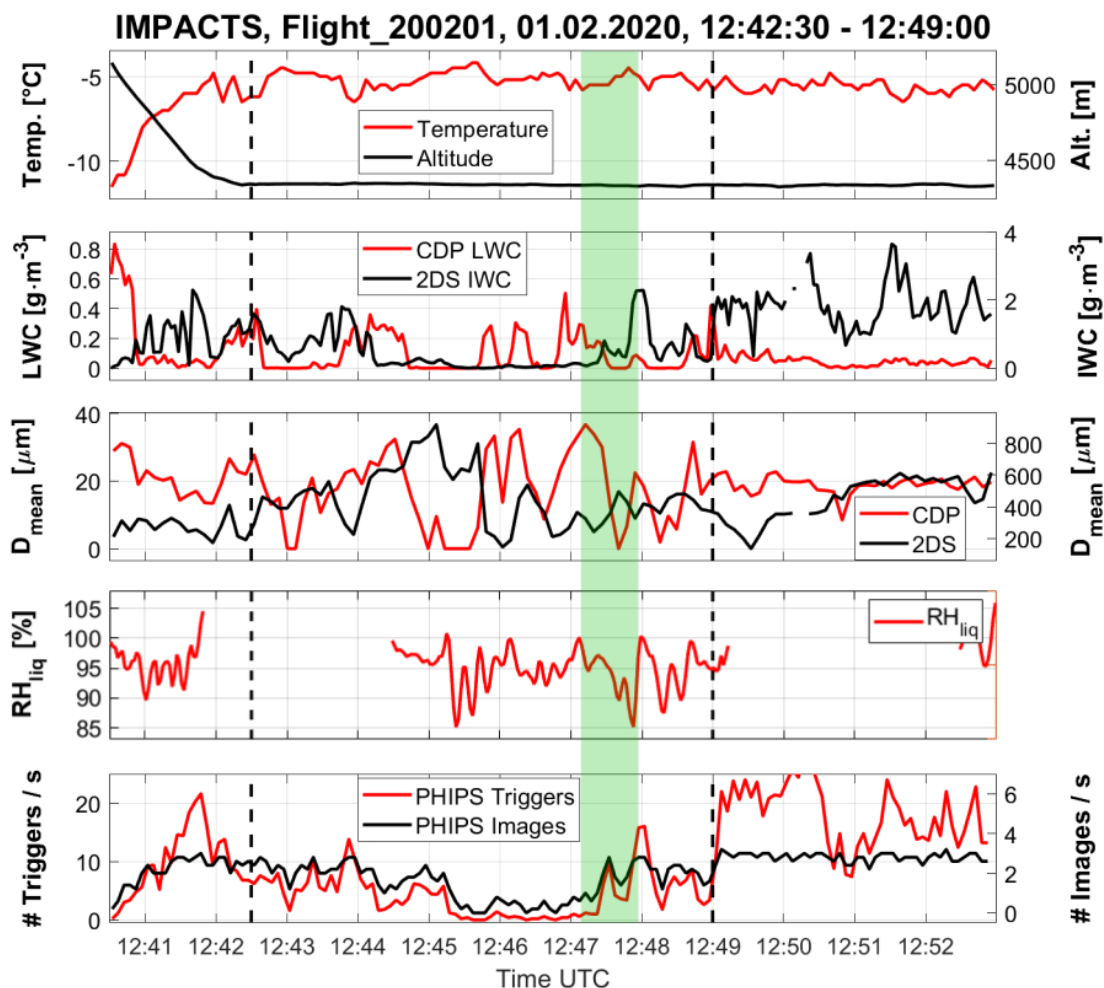
459 The trigger threshold of PHIPS was set in a way that the instrument started to trigger on droplets
 460 with diameters larger than $D > 100 \mu\text{m}$. In this segment, in total, 1,589 particles were triggered
 461 and 575 stereo images were acquired. Examples of ~~stereo~~ micrographs of particles from this flight
 462 segment are shown in Fig. ~~10b~~ 11. Of the 575 stereo images, 259 (45%) were not classified since
 463 they were identified as potential shattering fragments smaller than $D = 100 \mu\text{m}$. Shattering artifacts
 464 can be identified from the PHIPS stereo images that have a field of view of approx. $2.19 \text{ mm} \times$
 465 1.65 mm by looking for satellite particles. Even though shattering fragments do not always appear
 466 as “satellites” but can be found as single fragments within the image frame. Such individual
 467 shattering fragments can be typically identified as having sharp edges and a shape that does not
 468 appear to resemble that of a typical vapor grown crystal (i.e. a lack of hexagonal symmetry of
 469 the crystal facets). If such particles were identified during the manual image inspection, they were
 470 also categorized as shattering cases. Of the remaining ice particles (320) most are classified as

471 columnar particles (173) and 33 as needles. These particles show a wide spectrum of riming
472 degree, ranging from unrimed (43) to slightly (44), moderately (42) and heavily rimed particles
473 (124). We see different "types" of riming, most are epitaxially rimed (87), 56 show normal riming.
474 Furthermore, we see numerous particles with evidence of both normal and epitaxial riming on the
475 same particle (20), which we refer to as *mixed riming* in the following. Apart from that, we see
476 presence of 3 large drizzle droplets with diameters 200-300 μm as well as rimed dendrites (30)
477 and graupel (48) particles. 35 particles were classified as irregulars. Similar particle shapes are
478 observed on the CPI imagery (not shown here).

488 The lower panel of Fig. 12 shows four exemplary ice particles that were sampled within a 45 s
489 window (12:47:07 - 12:47:52 UTC, corresponding to a distance of 6.7 km) that is indicated by the
490 shaded green area in Fig. 10. The particles that were sampled within this period show columnar
491 particles during different stages of the riming process: an unrimed (a), a normally rimed (b), a
492 mixed rimed (c) and epitaxially rimed column (d). Since we observe normal and epitaxial riming
493 not only within the same segment in near spatial vicinity, but also on the same singular particles,
494 we argue that normal and epitaxial riming are, as hypothesized, interlinked. As proposed by
495 Korolev et al. (2020), we argue that epitaxial riming is the result of the ageing (deposition growth)
496 of normally rimed particles as sketched in the upper panel of Fig. 12: An unrimed ice particle
497 (a) accretes a supercooled droplet and forms the initial primary "normal" riming (b). Ambient
498 water vapour deposits on the rime matching the lattice structure of the underlying particle and thus
499 forming the faceted surface. ~~It is further possible that older rime grows on the expense of recently
500 accreted droplets that partly evaporate due to latent heat during the freezing process.~~ More droplets
501 are accreted such that normal and epitaxial riming can be observed on the same particle (c). The
502 process repeats and the particle grows further until, eventually, the whole surface is covered by
503 epitaxial rime (d).

508 5. Summary and Conclusion

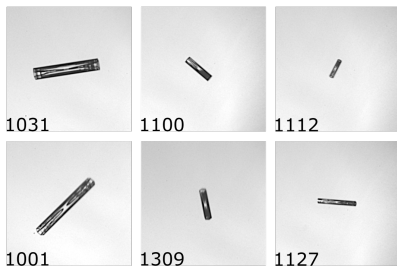
509 In this work, we have presented in-situ observations using the PHIPS probe during three aircraft
510 campaigns targeting MPCs in the Arctic, the Southern Ocean and US east coast. We have shown
511 that riming is prevalent in the sampled clouds. We have manually classified ice particles in a
512 size range from $100 \leq D \leq 700 \mu\text{m}$ and in the temperature range between $-17^\circ\text{C} \leq T \leq 0^\circ\text{C}$ regarding



479 FIG. 10. Example of PHIPS data acquired in a mixed-phase cloud near the US east coast sampled dur-
 480 ing the IMPACTS campaign on February 1st, 2020. Left: The graph shows an overview of meteorological
 481 parameters temperature, altitude, CDP liquid water content, 2D-S total water content, CDP and 2D-S number-
 482 weighed mean particle diameter and number of PHIPS images and total triggers. Right: Corresponding
 483 representative PHIPS images of particles sampled during the this segment marked by the dashed black lines are
 484 shown in Fig. 11 The green shaded area marks a 45 s segment during which the four particles shown in Fig. 12
 485 were acquired.

513 their riming status (rimed or unrimed) and surface riming degree (SRD). We show that riming is
 514 most prevalent at temperatures around -7°C , where, on average, 43% of the investigated particles
 515 showed evidence of riming. We show that riming fraction increases with ice particle size ($<20\%$

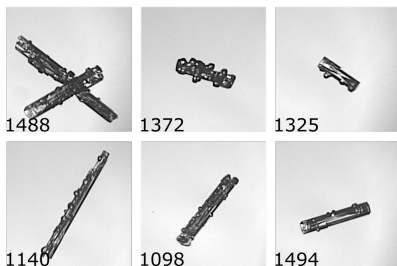
Unrimed



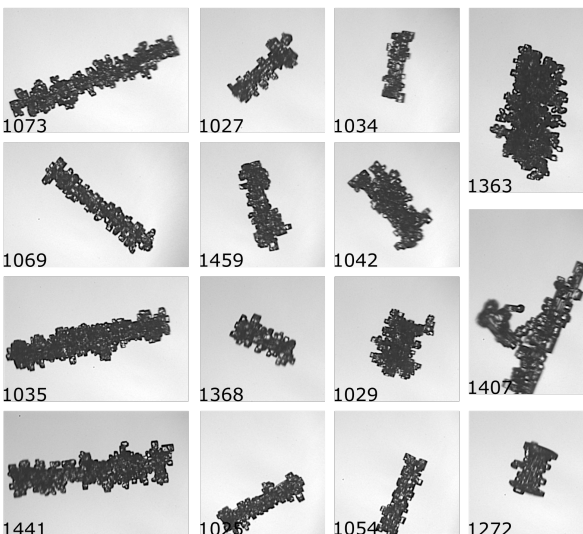
Slight Epitaxial Rimming



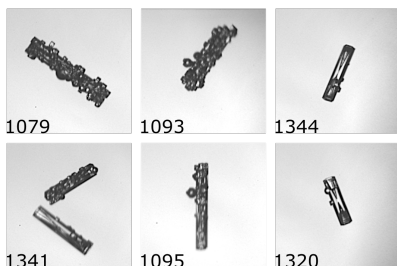
Normal Rimming



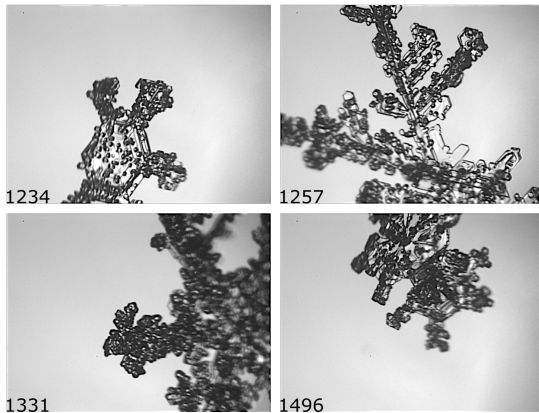
Heavy Epitaxial Rimming



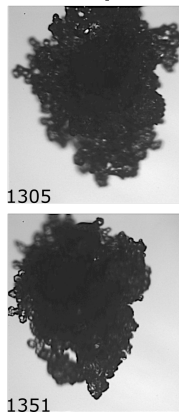
Mixed



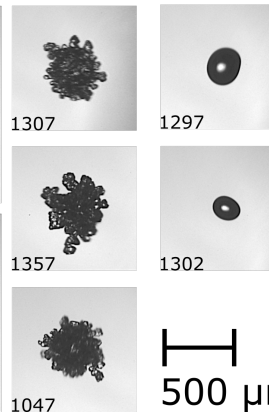
Rimmed Dendrites



Graupel

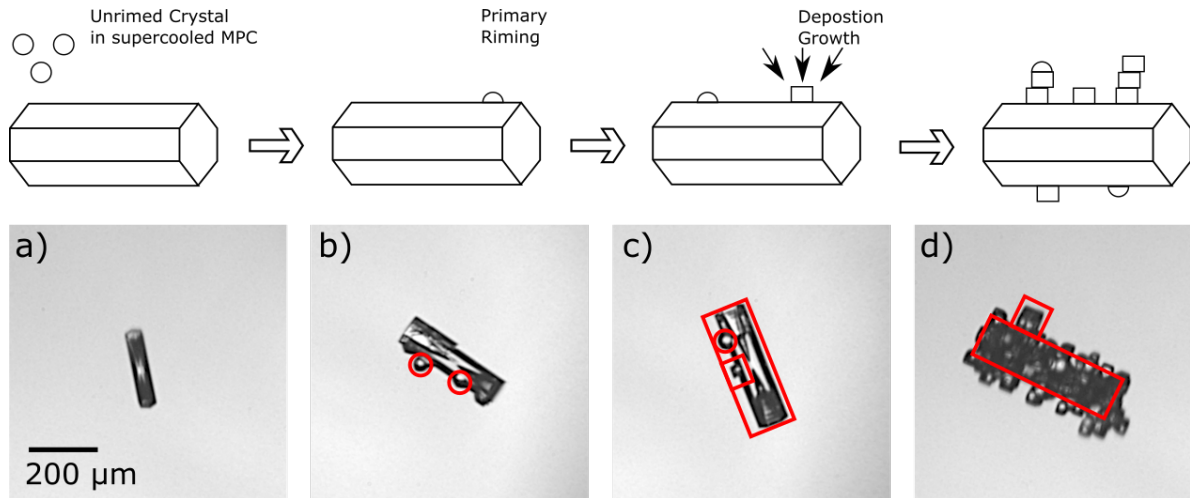


Drizzle



500 μ m

486 FIG. 11. [Corresponding representative PHIPS images of particles sampled during the segment indicated by](#)
487 [the dashed black lines in in Fig. 10. The numbers in the bottom left denote the image number.](#)



504 FIG. 12. Schematic sketch of an epitaxially rimed column during different stages of the ageing process: unrimed
 505 (a), normally rimed (b), mixed (c), and epitaxially rimed column (d). The lower panel shows corresponding
 506 exemplary PHIPS images (#1309, #1325, #1320, and #1368) acquired within a 45 s segment in the presented
 507 case-study (shaded green area in Fig. 10).

516 for $D \leq 200 \mu\text{m}$, 35-40% for $D \leq 400 \mu\text{m}$) and liquid water content (25% for $\text{LWC} \leq 0.05 \text{ g m}^{-3}$, up
 517 to 60% for $\text{LWC} = 0.5 \text{ g m}^{-3}$).

518 We investigated riming features such as surface riming degree, size of ~~rimed droplets~~ rime
 519 particles and one-sided riming based on visual inspection of individual stereo-images of ice
 520 ~~particles~~ crystals imaged by PHIPS during these campaigns. We show that the surface riming
 521 degree increases with decreasing temperature and increasing ice particle size.

522 Furthermore, we have described ice particles with faceted, crystalline build-up which is aligned
 523 to the lattice structure of the underlying particle. We call this "epitaxial riming" that we differentiate
 524 from the round "normal riming". Epitaxial riming is most notable in the temperature range from
 525 $-10^\circ\text{C} \leq T \leq 0^\circ\text{C}$ where epitaxial riming is visible on 32-37% of all rimed particles. We have
 526 presented a case study that demonstrates that normal and epitaxial riming can be observed in
 527 the same cloud segments and even simultaneously on the same single ice particles. We argue
 528 that epitaxially rimed particles are the result of deposition growth of water vapor on primarily
 529 rimed particles during their ageing process. However, further studies are needed to investigate
 530 the exact growth mechanisms of epitaxial riming, for example in laboratory studies. Furthermore,

531 implications of epitaxial riming are still unclear. For example, it is unclear if epitaxial riming
532 affects rime splintering process and the splinter production rate.

533 Currently, the implications of riming towards the climate are not yet well understood as most
534 present day climate prediction models lack a parameterization of riming and consider riming
535 only for large particles ($D \geq 1$ mm) in the sense of graupel and snow. Riming on smaller par-
536 ticles is usually not considered. The presented correlation between riming fraction and ambient
537 ~~meteorological~~microphysical parameters can be used as a basis for first steps towards such a riming
538 parameterization for small or large scale models.

539 *Acknowledgments.* We express our gratitude all participants of the field studies for their efforts,
540 in particular the technical crew of the AWI Polar 6, NSF G-V and NASA P3. We would like to
541 acknowledge operational, technical and scientific support provided by NCAR's Earth Observing
542 Laboratory, sponsored by the National Science Foundation. We thank Ulrike Romatschke for her
543 valuable help with the HCR data. We would also like to thank the technical and scientific staff
544 of IMK-AAF for their continuous support. We also thank Alexei Korolev and an anonymous
545 reviewer who provided valuable feedback that improved and clarified the manuscript.
546 This work has received funding from the Helmholtz Research Program Atmosphere and Climate,
547 by the German Research Foundation (DFG ~~grant-grants~~ JA 2818/1-1 and SCHN 1140/3-1) and the
548 Helmholtz Association's Initiative and Networking Fund (grant agreement no. VH-NG-1531).

549 *Data availability statement.* The PHIPS single particle scattering data can be found online in
550 the PANGAEA database (<https://doi.org/10.1594/PANGAEA.902611>) for ACLOUD and the
551 EOL database (<https://doi.org/10.5065/D6639NKQ>) for SOCRATES. The single particle
552 microscopic stereo images from those two campaigns are available upon request from the authors.
553 The single particle microscopic stereo images from the IMPACTS campaign can be found in the
554 GHVR DAAC database (<http://dx.doi.org/10.5067/IMPACTS/PHIPS/DATA101>)

555 **References**

556 Abdelmonem, A., E. Järvinen, D. Duft, E. Hirst, S. Vogt, T. Leisner, and M. Schnaiter, 2016:
557 Phips-halo: the airborne particle habit imaging and polar scattering probe – part 1: Design and
558 operation. *Atmospheric Measurement Techniques*, **9** (7), 3131–3144, [https://doi.org/10.5194/](https://doi.org/10.5194/amt-9-3131-2016)
559 [amt-9-3131-2016](https://doi.org/10.5194/amt-9-3131-2016), URL <https://www.atmos-meas-tech.net/9/3131/2016/>.

560 Baltensperger, U., M. Schwikowski, D. Jost, S. Nyeki, H. Gäggeler, and O. Poulida, 1998: Scav-
561 enging of atmospheric constituents in mixed phase clouds at the high-alpine site jungfrau-
562 joch part i: Basic concept and aerosol scavenging by clouds. *Atmospheric Environment*,
563 **32 (23)**, 3975–3983, [https://doi.org/https://doi.org/10.1016/S1352-2310\(98\)00051-X](https://doi.org/https://doi.org/10.1016/S1352-2310(98)00051-X), URL
564 <https://www.sciencedirect.com/science/article/pii/S135223109800051X>.

565 Blahak, U., and A. Seifert, 2015: Cosmo / clm / art training course, langen, march 2015. URL
566 https://www.hzg.de/imperia/md/assets/clm/neu5_tl3.pdf.

567 Brintjes, R. T., A. J. Heymsfield, and T. W. Krauss, 1987: An examination of double-plate ice crys-
568 tals and the initiation of precipitation in continental cumulus clouds. *Journal of Atmospheric Sci-*
569 *ences*, **44 (9)**, 1331 – 1350, [https://doi.org/10.1175/1520-0469\(1987\)044<1331:AEODPI>2.0.](https://doi.org/10.1175/1520-0469(1987)044<1331:AEODPI>2.0.CO;2)
570 [CO;2](https://doi.org/10.1175/1520-0469(1987)044<1331:AEODPI>2.0.CO;2), URL [https://journals.ametsoc.org/view/journals/atsc/44/9/1520-0469_1987_044_1331_](https://journals.ametsoc.org/view/journals/atsc/44/9/1520-0469_1987_044_1331_aeodpi_2_0_co_2.xml)
571 [aeodpi_2_0_co_2.xml](https://journals.ametsoc.org/view/journals/atsc/44/9/1520-0469_1987_044_1331_aeodpi_2_0_co_2.xml).

572 Bryant, G., J. Hallett, and B. Mason, 1960: The epitaxial growth of ice on single-crystalline
573 substrates. *Journal of Physics and Chemistry of Solids*, **12 (2)**, 189–IN18, [https://doi.org/https://doi.org/10.1016/0022-3697\(60\)90036-6](https://doi.org/https://doi.org/10.1016/0022-3697(60)90036-6), URL [https://www.sciencedirect.com/science/article/](https://www.sciencedirect.com/science/article/pii/0022369760900366)
574 [pii/0022369760900366](https://www.sciencedirect.com/science/article/pii/0022369760900366).

575

576 Diao, M., 2021: Vcsel 25hz water vapor data. version 2.0. UCAR/NCAR - Earth Ob-
577 serving Laboratory, URL <https://data.eol.ucar.edu/dataset/552.052>, [https://doi.org/10.26023/](https://doi.org/10.26023/V925-2H41-SD0F)
578 [V925-2H41-SD0F](https://doi.org/10.26023/V925-2H41-SD0F).

579 Ehrlich, A., and Coauthors, 2019: Collection of data sources for the Arctic CLOUD Observations
580 Using airborne measurements during polar Day (ACLOUD) campaign, North-West of Svalbard
581 between 23 May - 26 June 2017. PANGAEA, URL <https://doi.org/10.1594/PANGAEA.902603>,
582 <https://doi.org/10.1594/PANGAEA.902603>.

583 EOL, 2018: Socrates: Southern ocean clouds radiation aerosol transport experimental
584 study. UCAR/NCAR - Earth Observing Laboratory, URL [https://data.eol.ucar.edu/project/](https://data.eol.ucar.edu/project/SOCRATES)
585 [SOCRATES](https://data.eol.ucar.edu/project/SOCRATES).

586 Fan, J., S. Ghan, M. Ovchinnikov, X. Liu, P. J. Rasch, and A. Korolev, 2011: Rep-
587 resentation of arctic mixed-phase clouds and the wegener-bergeron-findeisen process in

588 climate models: Perspectives from a cloud-resolving study. *Journal of Geophysical*
589 *Research: Atmospheres*, **116 (D1)**, [https://doi.org/https://doi.org/10.1029/2010JD015375](https://doi.org/10.1029/2010JD015375),
590 URL <https://agupubs.onlinelibrary.wiley.com/doi/abs/10.1029/2010JD015375>, <https://agupubs.onlinelibrary.wiley.com/doi/pdf/10.1029/2010JD015375>.
591

592 Field, P. R., and Coauthors, 2017: *Secondary Ice Production - current state of the science and rec-*
593 *ommendations for the future*, Meteorological Monographs, Vol. 58, 7.1–7.20. American Mete-
594 orological Society, Boston (MA), <https://doi.org/10.1175/AMSMONOGRAPHS-D-16-0014.1>,
595 12.01.01; LK 01.

596 Garrett, T. J., and S. E. Yuter, 2014: Observed influence of riming, temperature, and tur-
597 bulence on the fallspeed of solid precipitation. *Geophysical Research Letters*, **41 (18)**,
598 6515–6522, [https://doi.org/https://doi.org/10.1002/2014GL061016](https://doi.org/10.1002/2014GL061016), URL <https://agupubs.onlinelibrary.wiley.com/doi/abs/10.1002/2014GL061016>, <https://agupubs.onlinelibrary.wiley.com/doi/pdf/10.1002/2014GL061016>.
599
600

601 Hallett, J., and S. C. Mossop, 1974: Production of secondary ice particles during
602 the riming process. *Nature*, **249 (5452)**, 26–28, [https://doi.org/https://doi.org/10.1038/](https://doi.org/10.1038/249026a0)
603 [249026a0](https://doi.org/10.1038/249026a0), URL <https://rmets.onlinelibrary.wiley.com/doi/abs/10.1002/qj.49710042514>, <https://rmets.onlinelibrary.wiley.com/doi/pdf/10.1002/qj.49710042514>.
604

605 Harimaya, T., 1975: The riming properties of snow crystals. *Journal of the Meteorological Society*
606 *of Japan. Ser. II*, **53 (6)**, 384–392, https://doi.org/10.2151/jmsj1965.53.6_384.

607 Hegg, D. A., A. D. Clarke, S. J. Doherty, and J. Ström, 2011: Measurements of black carbon aerosol
608 washout ratio on svalbard. *Tellus B*, **63 (5)**, 891–900, [https://doi.org/https://doi.org/10.1111/](https://doi.org/10.1111/j.1600-0889.2011.00577.x)
609 [j.1600-0889.2011.00577.x](https://doi.org/10.1111/j.1600-0889.2011.00577.x), URL [https://onlinelibrary.wiley.com/doi/abs/10.1111/j.1600-0889.](https://onlinelibrary.wiley.com/doi/abs/10.1111/j.1600-0889.2011.00577.x)
610 [2011.00577.x](https://onlinelibrary.wiley.com/doi/pdf/10.1111/j.1600-0889.2011.00577.x), <https://onlinelibrary.wiley.com/doi/pdf/10.1111/j.1600-0889.2011.00577.x>.

611 Herzegh, P. H., and P. V. Hobbs, 1980: The mesoscale and microscale structure and organization
612 of clouds and precipitation in midlatitude cyclones. ii: Warm-frontal clouds. *Journal of At-*
613 *mospheric Sciences*, **37 (3)**, 597 – 611, [https://doi.org/10.1175/1520-0469\(1980\)037<0597:](https://doi.org/10.1175/1520-0469(1980)037<0597:TMAMSA>2.0.CO;2)
614 [TMAMSA>2.0.CO;2](https://doi.org/10.1175/1520-0469(1980)037<0597:TMAMSA>2.0.CO;2), URL [https://journals.ametsoc.org/view/journals/atsc/37/3/1520-0469_](https://journals.ametsoc.org/view/journals/atsc/37/3/1520-0469_1980_037_0597_tmamsa_2_0_co_2.xml)
615 [1980_037_0597_tmamsa_2_0_co_2.xml](https://journals.ametsoc.org/view/journals/atsc/37/3/1520-0469_1980_037_0597_tmamsa_2_0_co_2.xml).

616 Järvinen, E., and Coauthors, 2018: Additional global climate cooling by clouds due to ice crystal
617 complexity. *Atmospheric Chemistry and Physics*, **18** (21), 15 767–15 781, <https://doi.org/10.5194/acp-18-15767-2018>, URL <https://www.atmos-chem-phys.net/18/15767/2018/>.

619 Järvinen, E., and Coauthors, 2021: Ice crystal complexity and link to cirrus cloud radiative effect.
620 *Journal of Geophysical Research: Atmospheres*, **2021**, in review.

621 Keppas, S. C., J. Crosier, T. W. Choularton, and K. N. Bower, 2017: Ice lollies: An ice
622 particle generated in supercooled conveyor belts. *Geophysical Research Letters*, **44** (10),
623 5222–5230, <https://doi.org/10.1002/2017GL073441>, URL <https://agupubs.onlinelibrary.wiley.com/doi/abs/10.1002/2017GL073441>, <https://agupubs.onlinelibrary.wiley.com/doi/pdf/10.1002/2017GL073441>.

626 Khain, A., A. Pokrovsky, and I. Sednev, 1999: Some effects of cloud–aerosol interaction on cloud
627 microphysics structure and precipitation formation: numerical experiments with a spectral
628 microphysics cloud ensemble model. *Atmospheric Research*, **52** (3), 195–220, [https://doi.org/10.1016/S0169-8095\(99\)00027-7](https://doi.org/10.1016/S0169-8095(99)00027-7), URL <https://www.sciencedirect.com/science/article/pii/S0169809599000277>.

631 Kikuchi, K., and H. Uyeda, 1979: Cloud droplets and rain drops collected and frozen on nat-
632 ural snow crystals. *Journal of the Meteorological Society of Japan. Ser. II*, **57** (3), 273–281,
633 https://doi.org/10.2151/jmsj1965.57.3_273.

634 Kiselev, A., F. Bachmann, P. Pedevilla, S. J. Cox, A. Michaelides, D. Gerthsen, and T. Leisner,
635 2016: Active sites in heterogeneous ice nucleation—the example of k-rich feldspars. *Science*,
636 <https://doi.org/10.1126/science.aai8034>, URL <https://science.sciencemag.org/content/early/2016/12/07/science.aai8034>, <https://science.sciencemag.org/content/early/2016/12/07/science.aai8034.full.pdf>.

639 Kneifel, S., and D. Moisseev, 2020: Long-term statistics of riming in nonconvective clouds derived
640 from ground-based doppler cloud radar observations. *Journal of the Atmospheric Sciences*,
641 **77** (10), 3495 – 3508, <https://doi.org/10.1175/JAS-D-20-0007.1>, URL <https://journals.ametsoc.org/view/journals/atsc/77/10/jasD200007.xml>.

643 Knudsen, E. M., and Coauthors, 2018: Meteorological conditions during the acloud/pascal
644 field campaign near svalbard in early summer 2017. *Atmospheric Chemistry and Physics*,
645 **18** (24), 17 995–18 022, <https://doi.org/10.5194/acp-18-17995-2018>, URL [https://www.
646 atmos-chem-phys.net/18/17995/2018/](https://www.atmos-chem-phys.net/18/17995/2018/).

647 Korolev, A., and Coauthors, 2017: Mixed-phase clouds: Progress and challenges. *Meteoro-
648 logical Monographs*, **58**, 5.1–5.50, [https://doi.org/10.1175/AMSMONOGRAPHIS-D-17-0001.
649 1](https://doi.org/10.1175/AMSMONOGRAPHIS-D-17-0001.1), URL [https://doi.org/10.1175/
650 AMSMONOGRAPHIS-D-17-0001.1](https://doi.org/10.1175/AMSMONOGRAPHIS-D-17-0001.1).

651 Korolev, A., and Coauthors, 2020: A new look at the environmental conditions favorable to sec-
652 ondary ice production. *Atmospheric Chemistry and Physics*, **20** (3), 1391–1429, [https://doi.org/
653 10.5194/acp-20-1391-2020](https://doi.org/10.5194/acp-20-1391-2020), URL <https://acp.copernicus.org/articles/20/1391/2020/>.

654 Leinonen, J., and W. Szyrmer, 2015: Radar signatures of snowflake riming: A
655 modeling study. *Earth and Space Science*, **2** (8), 346–358, [https://doi.org/https://doi.
656 org/10.1002/2015EA000102](https://doi.org/https://doi.org/10.1002/2015EA000102), URL [https://agupubs.onlinelibrary.wiley.com/doi/abs/10.1002/
657 2015EA000102](https://agupubs.onlinelibrary.wiley.com/doi/abs/10.1002/2015EA000102), <https://agupubs.onlinelibrary.wiley.com/doi/pdf/10.1002/2015EA000102>.

658 Leinonen, J., and Coauthors, 2018: Retrieval of snowflake microphysical properties from mul-
659 tiframe radar observations. *Atmospheric Measurement Techniques*, **11** (10), 5471–5488,
660 <https://doi.org/10.5194/amt-11-5471-2018>, URL [https://amt.copernicus.org/articles/11/5471/
661 2018/](https://amt.copernicus.org/articles/11/5471/2018/).

662 Libbrecht, K., 2016: *Ken Libbrecht's Field Guide to Snowflakes*. Voyageur Press, URL [https:
663 //books.google.de/books?id=eOv83aUgOvwC](https://books.google.de/books?id=eOv83aUgOvwC).

664 Libbrecht, K., C. Miller, R. Potter, N. Budaeva, C. Lemon, and S. Thomas, 2015: Toward a
665 comprehensive model of snow crystal growth: 4. measurements of diffusion-limited growth at
666 -15 c.

667 Lin, Y., L. Donner, and B. Colle, 2011: Parameterization of riming intensity and its impact on ice
668 fall speed using arm data. *Monthly Weather Review - MON WEATHER REV*, **139**, 1036–1047,
669 <https://doi.org/10.1175/2010MWR3299.1>.

670 Locatelli, J. D., and P. V. Hobbs, 1974: Fall speeds and masses of solid precipitation
671 particles. *Journal of Geophysical Research (1896-1977)*, **79 (15)**, 2185–2197, [https://doi.org/
672 https://doi.org/10.1029/JC079i015p02185](https://doi.org/https://doi.org/10.1029/JC079i015p02185), URL [https://agupubs.onlinelibrary.wiley.com/doi/
673 abs/10.1029/JC079i015p02185](https://agupubs.onlinelibrary.wiley.com/doi/abs/10.1029/JC079i015p02185), [https://agupubs.onlinelibrary.wiley.com/doi/pdf/10.1029/
674 JC079i015p02185](https://agupubs.onlinelibrary.wiley.com/doi/pdf/10.1029/JC079i015p02185).

675 Magono, C., and H. Aburakawa, 1969: Experimental studies on snow crystals of plane type with
676 spatial branches. *Journal of the Faculty of Science, Hokkaido University. Series 7, Geophysics*,
677 **3 (2)**, 85–97, URL <http://hdl.handle.net/2115/8680>.

678 Magono, C., and C. W. Lee, 1966: Meteorological classification of natural snow crystals. *Journal*
679 *of the Faculty of Science, Hokkaido University. Series 7, Geophysics*, **2 (4)**, 321–335, URL
680 <http://hdl.handle.net/2115/8672>.

681 Martin, M. Y., and R. Bennett, 2020: P-3 meteorological and navigation data impacts. NASA
682 Global Hydrometeorology Resource Center DAAC, URL [https://ghrc.nsstc.nasa.gov/hydro/
683 details/p3metnavimpacts](https://ghrc.nsstc.nasa.gov/hydro/details/p3metnavimpacts), <https://doi.org/10.5067/IMPACTS/P3/DATA101>.

684 Mason, S. L., C. J. Chiu, R. J. Hogan, D. Moisseev, and S. Kneifel, 2018: Retrievals of riming
685 and snow density from vertically pointing doppler radars. *Journal of Geophysical Research:*
686 *Atmospheres*, **123 (24)**, 13,807–13,834, <https://doi.org/https://doi.org/10.1029/2018JD028603>,
687 URL <https://agupubs.onlinelibrary.wiley.com/doi/abs/10.1029/2018JD028603>, [https://agupubs.
688 onlinelibrary.wiley.com/doi/pdf/10.1029/2018JD028603](https://agupubs.onlinelibrary.wiley.com/doi/pdf/10.1029/2018JD028603).

689 McCoy, D. T., I. Tan, D. L. Hartmann, M. D. Zelinka, and T. Storelvmo,
690 2016: On the relationships among cloud cover, mixed-phase partitioning, and
691 planetary albedo in gcms. *Journal of Advances in Modeling Earth Systems*,
692 **8 (2)**, 650–668, <https://doi.org/10.1002/2015MS000589>, URL [https://agupubs.onlinelibrary.
693 wiley.com/doi/abs/10.1002/2015MS000589](https://agupubs.onlinelibrary.wiley.com/doi/abs/10.1002/2015MS000589), [https://agupubs.onlinelibrary.wiley.com/doi/pdf/
694 10.1002/2015MS000589](https://agupubs.onlinelibrary.wiley.com/doi/pdf/10.1002/2015MS000589).

695 McFarquhar, G. M., and Coauthors, 2019: Airborne, ship-, and ground-based observations of
696 clouds, aerosols, and precipitation from recent field projects over the southern ocean. *99th an-
697 nual meeting, American Meteorological Society*, URL [https://ams.confex.com/ams/2019Annual/
698 meetingapp.cgi/Paper/350863](https://ams.confex.com/ams/2019Annual/meetingapp.cgi/Paper/350863).

- 699 McMurdie, L., G. Heymsfield, J. Yorks, and S. Braun, 2019: Investigation of microphysics and
700 precipitation for atlantic coast-threatening snowstorms (impacts) collection. NASA EOSDIS
701 Global Hydrology Resource Center Distributed, Active Archive Center, Huntsville, Alabama,
702 U.S.A., URL <http://dx.doi.org/10.5067/IMPACTS/DATA101>.
- 703 Mizuno, Y., 1984: Epitaxial freezing of supercooled droplets on ice surfaces. *Contributions from*
704 *the Institute of Low Temperature Science*, **A33**, 1–27, URL <http://hdl.handle.net/2115/20248>.
- 705 Mizuno, Y., and G. Wakahama, 1983: Structure and orientation of frozen droplets on ice surfaces.
706 *The Journal of Physical Chemistry*, **87 (21)**, 4161–4167, <https://doi.org/10.1021/j100244a037>,
707 URL <https://doi.org/10.1021/j100244a037>, <https://doi.org/10.1021/j100244a037>.
- 708 Mosimann, L., 1995: An improved method for determining the degree of snow crystal
709 riming by vertical doppler radar. *Atmospheric Research*, **37 (4)**, 305–323, [https://doi.org/https://doi.org/10.1016/0169-8095\(94\)00050-N](https://doi.org/https://doi.org/10.1016/0169-8095(94)00050-N), URL <https://www.sciencedirect.com/science/article/pii/016980959400050N>.
- 712 Mosimann, L., M. Steiner, J. Collett, and et al., 1993: Ice crystal observations and the degree
713 of riming in winter precipitation. *Water Air Soil Pollution*, **68**, 29–42, <https://doi.org/https://doi.org/10.1007/BF00479391>.
- 715 Mosimann, L., E. Weingartner, and A. Waldvogel, 1994: An analysis of accreted
716 drop sizes and mass on rimed snow crystals. *Journal of Atmospheric Sciences*,
717 **51 (11)**, 1548 – 1558, [https://doi.org/10.1175/1520-0469\(1994\)051<1548:AAOADS>2.0.CO;](https://doi.org/10.1175/1520-0469(1994)051<1548:AAOADS>2.0.CO;2)
718 **2**, URL [https://journals.ametsoc.org/view/journals/atsc/51/11/1520-0469_1994_051_1548_](https://journals.ametsoc.org/view/journals/atsc/51/11/1520-0469_1994_051_1548_aoads_2_0_co_2.xml)
719 [aoads_2_0_co_2.xml](https://journals.ametsoc.org/view/journals/atsc/51/11/1520-0469_1994_051_1548_aoads_2_0_co_2.xml).
- 720 Ono, A., 1969: The shape and riming properties of ice crystals in natural clouds. *Journal of At-*
721 *mospheric Sciences*, **26 (1)**, 138 – 147, [https://doi.org/10.1175/1520-0469\(1969\)026<0138:](https://doi.org/10.1175/1520-0469(1969)026<0138:TSARPO>2.0.CO;2)
722 [TSARPO>2.0.CO;2](https://doi.org/10.1175/1520-0469(1969)026<0138:TSARPO>2.0.CO;2), URL [https://journals.ametsoc.org/view/journals/atsc/26/1/1520-0469_](https://journals.ametsoc.org/view/journals/atsc/26/1/1520-0469_1969_026_0138_tsarpo_2_0_co_2.xml)
723 [1969_026_0138_tsarpo_2_0_co_2.xml](https://journals.ametsoc.org/view/journals/atsc/26/1/1520-0469_1969_026_0138_tsarpo_2_0_co_2.xml).
- 724 Ovchinnikov, M., and Coauthors, 2014: Intercomparison of large-eddy simulations of
725 arctic mixed-phase clouds: Importance of ice size distribution assumptions. *Jour-*
726 *nal of Advances in Modeling Earth Systems*, **6 (1)**, 223–248, <https://doi.org/https://doi.org/10.1029/2013MS000888>.

727 org/10.1002/2013MS000282, URL <https://agupubs.onlinelibrary.wiley.com/doi/abs/10.1002/>
728 2013MS000282, <https://agupubs.onlinelibrary.wiley.com/doi/pdf/10.1002/2013MS000282>.

729 Pashley, D., 1956: The study of epitaxy in thin surface films. *Advances in Physics*,
730 **5 (18)**, 173–240, <https://doi.org/10.1080/00018735600101175>, URL [https://doi.org/10.1080/](https://doi.org/10.1080/00018735600101175)
731 00018735600101175, <https://doi.org/10.1080/00018735600101175>.

732 Pflaum, J. C., and H. R. Pruppacher, 1979: A wind tunnel investigation of the growth of
733 graupel initiated from frozen drops. *Journal of Atmospheric Sciences*, **36 (4)**, 680 – 689,
734 [https://doi.org/10.1175/1520-0469\(1979\)036<0680:AWTIOT>2.0.CO;2](https://doi.org/10.1175/1520-0469(1979)036<0680:AWTIOT>2.0.CO;2), URL [https://journals.](https://journals.ametsoc.org/view/journals/atsc/36/4/1520-0469_1979_036_0680_awtiot_2_0_co_2.xml)
735 [ametsoc.org/view/journals/atsc/36/4/1520-0469_1979_036_0680_awtiot_2_0_co_2.xml](https://journals.ametsoc.org/view/journals/atsc/36/4/1520-0469_1979_036_0680_awtiot_2_0_co_2.xml).

736 Rango, A., J. Foster, E. G. Josberger, E. F. Erbe, W. P. Wergin, and C. Pooley, 2003:
737 Rime and graupel: Description and characterization as revealed by low-temperature scan-
738 ning electron microscopy. *Scanning*, **25 (3)**, 121–131, [https://doi.org/https://doi.org/10.1002/](https://doi.org/https://doi.org/10.1002/sca.4950250304)
739 [sca.4950250304](https://doi.org/https://doi.org/10.1002/sca.4950250304), URL <https://onlinelibrary.wiley.com/doi/abs/10.1002/sca.4950250304>, <https://onlinelibrary.wiley.com/doi/pdf/10.1002/sca.4950250304>.

741 Romatschke, U., 2021: Melting layer detection and observation with the near airborne w-band
742 radar. *Remote Sensing*, **13 (9)**, <https://doi.org/10.3390/rs13091660>, URL [https://www.mdpi.](https://www.mdpi.com/2072-4292/13/9/1660)
743 [com/2072-4292/13/9/1660](https://www.mdpi.com/2072-4292/13/9/1660).

744 Romatschke, U., and M. Dixon, 2022: Vertically resolved convective/stratiform echo type identi-
745 fication and convectivity retrieval for vertically pointing radars. <https://doi.org/10.31223/x54s77>,
746 URL <https://doi.org/10.31223/x54s77>.

747 Saleeby, S. M., and W. R. Cotton, 2008: A binned approach to cloud-droplet riming imple-
748 mented in a bulk microphysics model. *Journal of Applied Meteorology and Climatology*, **47 (2)**,
749 694 – 703, <https://doi.org/10.1175/2007JAMC1664.1>, URL [https://journals.ametsoc.org/view/](https://journals.ametsoc.org/view/journals/apme/47/2/2007jamc1664.1.xml)
750 journals/apme/47/2/2007jamc1664.1.xml.

751 Schnaiter, M., E. Järvinen, A. Abdelmonem, and T. Leisner, 2018: Phips-halo: the airborne parti-
752 cle habit imaging and polar scattering probe – part 2: Characterization and first results. *Atmo-*
753 *spheric Measurement Techniques*, **11 (1)**, 341–357, <https://doi.org/10.5194/amt-11-341-2018>,
754 URL <https://www.atmos-meas-tech.net/11/341/2018/>.

755 Schnaiter, M., and Coauthors, 2016: Cloud chamber experiments on the origin of ice crystal com-
756 plexity in cirrus clouds. *Atmospheric Chemistry and Physics*, **16** (8), 5091–5110, [https://doi.org/](https://doi.org/10.5194/acp-16-5091-2016)
757 10.5194/acp-16-5091-2016, URL <https://acp.copernicus.org/articles/16/5091/2016/>.

758 Schön, R., and Coauthors, 2011: Particle habit imaging using incoherent light: A first step toward
759 a novel instrument for cloud microphysics. *Journal of Atmospheric and Oceanic Technology*,
760 **28** (4), 493–512, [https://doi.org/10.1175/](https://doi.org/10.1175/2011JTECHA1445.1)
761 2011JTECHA1445.1, [https://doi.org/10.1175/](https://doi.org/10.1175/2011JTECHA1445.1)
2011JTECHA1445.1, <https://doi.org/10.1175/2011JTECHA1445.1>.

762 Stevens, R. G., and Coauthors, 2018: A model intercomparison of ccn-limited tenuous clouds in
763 the high arctic. *Atmospheric Chemistry and Physics*, **18** (15), 11 041–11 071, [https://doi.org/](https://doi.org/10.5194/acp-18-11041-2018)
764 10.5194/acp-18-11041-2018, URL <https://acp.copernicus.org/articles/18/11041/2018/>.

765 Takahashi, C., 1979: Formation of poly-crystalline snow crystals by riming process. *Journal of the*
766 *Meteorological Society of Japan. Ser. II*, **57** (5), 458–464, [https://doi.org/10.2151/jmsj1965.57.](https://doi.org/10.2151/jmsj1965.57.5_458)
767 5_458.

768 UCAR/NCAR-Earth Observing Laboratory, 2019: Socrates: Low rate (lrt - 1 sps) navigation, state
769 parameter, and microphysics flight-level data. version 1.3. UCAR/NCAR - Earth Observing Lab-
770 oratory, URL <https://data.eol.ucar.edu/dataset/552.002>, <https://doi.org/10.5065/D6M32TM9>.

771 UCAR/NCAR-EOL, 2022: Near hcr radar and hsrl lidar moments data. version 3.0. ucar/ncar -
772 earth observing laboratory. URL <https://doi.org/10.5065/D68914PH>.

773 Uyeda, H., and K. Kikuchi, 1978: Freezing experiment of supercooled water droplets frozen by
774 using single crystal ice. *Journal of the Meteorological Society of Japan. Ser. II*, **56** (1), 43–51,
775 https://doi.org/10.2151/jmsj1965.56.1_43.

776 Uyeda, H., and K. Kikuchi, 1980: Measurements of the principal axis of frozen hemispheric water
777 droplets. *Journal of the Meteorological Society of Japan. Ser. II*, **58** (1), 52–58, [https://doi.org/](https://doi.org/10.2151/jmsj1965.58.1_52)
778 10.2151/jmsj1965.58.1_52.

779 Waitz, F., M. Schnaiter, T. Leisner, and E. Järvinen, 2021: Phips-halo: the airborne particle habit
780 imaging and polar scattering probe – part 3: Single particle phase discrimination and particle
781 size distribution based on angular scattering function. *Atmospheric Measurement Techniques*

782 *Discussions*, **2021**, 1–28, <https://doi.org/10.5194/amt-2020-297>, URL <https://amt.copernicus.org/preprints/amt-2020-297/>.

784 Wang, P. K., and W. Ji, 2000: Collision efficiencies of ice crystals at low–intermediate reynolds
785 numbers colliding with supercooled cloud droplets: A numerical study. *Journal of the At-*
786 *mospheric Sciences*, **57 (8)**, 1001 – 1009, [https://doi.org/10.1175/1520-0469\(2000\)057<1001:](https://doi.org/10.1175/1520-0469(2000)057<1001:CEOICA>2.0.CO;2)
787 [CEOICA>2.0.CO;2](https://doi.org/10.1175/1520-0469(2000)057<1001:CEOICA>2.0.CO;2), URL [https://journals.ametsoc.org/view/journals/atsc/57/8/1520-0469_](https://journals.ametsoc.org/view/journals/atsc/57/8/1520-0469_2000_057_1001_ceoica_2.0.co_2.xml)
788 [2000_057_1001_ceoica_2.0.co_2.xml](https://journals.ametsoc.org/view/journals/atsc/57/8/1520-0469_2000_057_1001_ceoica_2.0.co_2.xml).

789 Wendisch, M., A. Macke, A. Ehrlich, C. Lüpkes, and Coauthors, 2019: The arctic cloud puzzle:
790 Using acloud/pascal multiplatform observations to unravel the role of clouds and aerosol particles
791 in arctic amplification. *Bulletin of the American Meteorological Society*, **100 (5)**, 841–871,
792 <https://doi.org/10.1175/BAMS-D-18-0072.1>, URL [https://doi.org/10.1175/BAMS-D-18-0072.](https://doi.org/10.1175/BAMS-D-18-0072.1)
793 [1, https://doi.org/10.1175/BAMS-D-18-0072.1](https://doi.org/10.1175/BAMS-D-18-0072.1).

794 Ávila, E. E., N. E. Castellano, C. P. R. Saunders, R. E. Bürgesser, and G. G. Aguirre Varela,
795 2009: Initial stages of the riming process on ice crystals. *Geophysical Research Let-*
796 *ters*, **36 (9)**, [https://doi.org/https://doi.org/10.1029/2009GL037723](https://doi.org/10.1029/2009GL037723), URL [https://agupubs.](https://agupubs.onlinelibrary.wiley.com/doi/abs/10.1029/2009GL037723)
797 [onlinelibrary.wiley.com/doi/abs/10.1029/2009GL037723](https://agupubs.onlinelibrary.wiley.com/doi/abs/10.1029/2009GL037723), [https://agupubs.onlinelibrary.wiley.](https://agupubs.onlinelibrary.wiley.com/doi/pdf/10.1029/2009GL037723)
798 [com/doi/pdf/10.1029/2009GL037723](https://agupubs.onlinelibrary.wiley.com/doi/pdf/10.1029/2009GL037723).